



Prepared for:

European Union MAST-III SAFE



RWS-RIKZ

# Laboratory experiments on sediment dynamics and density gradation

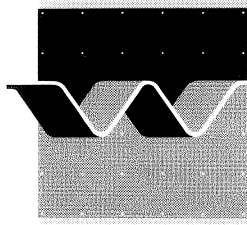
Part I: Time-averaged measurements

Data Report

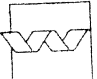
June 2000



Groningen State University-KVI (partner)



**wl | delft hydraulics**

	bibliotheek postbus 177 - 2500 MH Delft waterloorkundig laboratorium/WL
BB	60962
WL	H2305.73
EXPL	



R0007826

VERVALLEN  
VERVALLEN

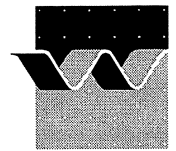
## Laboratory experiments on sediment dynamics and density gradation

Part I: Time-averaged measurements

Ronald Koomans and Judith Bosboom

Data Report

June 2000



**CLIENT:** European Union MAST-III SAFE  
&  
Rijkswaterstaat/Rijksinstituut voor Kust en Zee (RIKZ)

**TITLE:** Laboratory experiments on sediment dynamics and density gradation  
Part I: time-averaged measurements

**ABSTRACT:**

The data presented in this report were obtained and analysed within the framework of the EU-sponsored MAST-III SAFE project. The measurements of hydrodynamics, suspended sediment concentrations, sediment transport and radiometry were carried out on a natural 2DV beach under erosive conditions in WL|DELFT HYDRAULICS' Scheldt flume. Besides dune sand (series A), also various mixtures of dune sand and heavy minerals were used to investigate selective transport phenomena of minerals with a different density (series B through D). Time-mean sediment concentrations, radiometry (bed composition), bed profile evolution (data report part I: Time-averaged measurements (Koomans and Bosboom, 2000) and time-dependent measurements (surface elevations and time-dependent velocities and sediment concentrations at one elevation above the bed; data report part II: Time-dependent measurements (Bosboom and Koomans, 2000) were measured for all mixtures.

**REFERENCES:**

VER.	ORIGINATOR	DATE	REMARKS	REVIEW	APPROVED BY
1.0	J. Bosboom	15-6-00		M.J.F. Stive	T. Schilperoort

<b>PROJECT IDENTIFICATION:</b>								
<b>KEYWORDS:</b>								
<b>CONTENTS:</b>	<b>TEXT PAGES</b>	32	<b>TABLES</b>		<b>FIGURES</b>	5	<b>APPENDICES</b>	4
<b>STATUS:</b>	<input type="checkbox"/> PRELIMINARY	<input type="checkbox"/> DRAFT	<input checked="" type="checkbox"/> FINAL					

# Contents

1	Introduction	2
1.1	Background and aim of study	2
1.2	Outline of report	2
1.3	Acknowledgements	3
2	Experimental set-up	4
2.1	Scheldt flume	4
2.2	Measurement programme and acquisition of data	4
2.3	Steering and wave conditions	6
2.4	Sediment	6
2.5	Instrumentation and data acquisition	7
3	Instrumentation and calibration	12
3.1	PROVO	12
3.2	MEDUSA	13
3.3	Transverse suction system	15
3.4	Settling tube	17
3.5	BGO detector sample analyses (laboratory)	17
4	Data analysis and validation	22
4.1	Bed heights and sediment transport rates	22
4.2	Mean concentration	27
4.3	Grain-properties	28
4.4	Sediment composition	29
4.5	Sound	30
5	Conclusions and recommendations	31
6	References	33
 <b>APPENDIX A .</b>		<b>A-2</b>
1	Figures	A-3
 <b>APPENDIX B .</b>		<b>B-1</b>
1	Overview of measurements	B-2
 <b>APPENDIX C .</b>		<b>C-1</b>
1	Measurements of sediment composition	C-2
1.1	Introduction	C-2
1.2	Rendement	C-5
1.3	Model parameterisation	C-8
2	Calibration	C-12
3	Validation & calibration of the model	C-18
4	Validation of the calibration	C-20
5	Conclusions	C-24
6	References	C-25
 <b>APPENDIX D .</b>		<b>D-1</b>
1	The meaning of uncertainties and $\chi^2_{red}$	D-2



# I Introduction

## I.1 Background and aim of study

Within the framework of the EU-sponsored MAST-III SAFE project a programme of detailed measurements of hydrodynamics, sediment transport and radiometry has been carried out in DELFT HYDRAULICS' Scheldt flume.

The objective of the study was twofold: 1) the generation of high quality and high resolution data on hydrodynamics and sediment transport dynamics on a natural beach under erosive conditions with special attention to near-bottom resolution; and 2) the generation of data of selective transport phenomena of minerals which differ in density.

During the project, DELFT HYDRAULICS made available the Scheldt Flume and took care of expert assistance in running the facility and carrying out the experiments. The team from DELFT HYDRAULICS was led by J. Bosboom (project manager) and consisted of P. Pasterkamp and A. ter Veen. R. de Vries provided assistance for the operation of the experiments.

The team from the University of Groningen (KVI) consisted of R.L. Koomans assisted by several other researchers during different parts of the experiments: P.W. Groen, R. ten Have, P.G.H.M. Hendricks, J. Limburg and L.B. Venema. Two students of Delft University of Technology, L. Barends and W. Kuiper, assisted in the experiments. H. Demaie (Sogreah, France) assisted in the preparation of the final experiments.

The total duration of the project was four weeks (in August and September 1998), including the preparation of the Scheldt flume, the positioning and testing of the instruments. The actual experiments were carried out in 15 days.

## I.2 Outline of report

This data report consists of two parts: part I: Time-averaged measurements and part II: Time-dependent measurements (Bosboom and Koomans, 2000). The first two chapters of both reports are equal and aim to give an overview of the experimental set-up and the type of data that were collected. In chapter 3, a more elaborate discussion on the measuring techniques and calibration procedures is given. In part I, time-averaged measuring techniques and their calibration are presented while in part II the time dependent techniques are discussed. Chapter 4 of part I and II focuses on data validation and provides a discussion on the uncertainties in the time-averaged and time-dependent measurements respectively. Where necessary, results are shown, but detailed descriptions and interpretations of experimental data will not be given in this data report.

### **I.3 Acknowledgements**

This work is undertaken in the SAFE project, in the framework of the EU-sponsored Marine Science and Technology Programme (MAST-III), under contractno. MAS3-CT95-0004. It is cosponsored by the Dutch Ministry of Transport and Public Works (Rijkswaterstaat). This work is also part of the Nuclear Geophysics programme of the Kernfysisch Versneller Instituut, Rijksuniversiteit Groningen and the Netherlands Centre of Coastal research.

## 2 Experimental set-up

### 2.1 Scheldt flume

The experiments were carried out in DELFT HYDRAULICS' Scheldt flume, location the Voorst. This facility has a length of 55 m, a width of 1.0 m and a total depth of 1.2 m. The facility consists of a concrete/iron bottom and glass walls. For the location of the instruments in the facility we adopted the following co-ordinate system (see also Figure 2.1) :

- the x-direction was parallel to the channel axis, the positive x-direction was from the wave-board towards the “beach face”, and  $x=0$  was located at the mean position of the wave board.
- the y-direction was in the horizontal plane parallel to the channel bed and orthogonal to the x-direction. The positive y-direction was then to the right when looking from the wave board to the “beach face”, and  $y=0$  was located inside the channel at the glass window to the left. For practical reasons, the two sides of the flume were named as D (“drukleiding”) and W (“wand”)-side. The D-side is located at  $y=1\text{m}$ , the W-side is located at  $y=0\text{m}$ .
- the z-direction was directed vertically upward, with  $z=0$  located at the top of the concrete bed being the horizontal bottom part of the flume.

### 2.2 Measurement programme and acquisition of data

#### Measurement programme

The measurement programme globally consisted of four series (see Table 2.1):

In series A special attention was paid to high-resolution measurements of hydrodynamics and sediment transport. the focus was on the collection of instantaneous velocity and concentration measurements at several locations along the beach profile, for varying distances above the sandy bed.

These experiments were carried out on an initially plane, with a slope of 1 in 40, beach consisting of dune sand (see Figure 2.1). During the operation observables were measured by a number of instruments attached to a movable carriage (see section 2.5). Moreover, four wave-gauges at a fixed position in the flume throughout the experimental programme, measured the water elevation. The instruments on the carriage measured at a fixed horizontal and vertical position for about half an hour and were then moved to other locations. The sediment profile was measured at several time periods between runs.

Series B focussed on the selective transport of placers of Zircon. Thin layers of Zircon were placed at several x-positions on the single-barred final profile of series A. In these experiments only the sediment profile and composition was measured.

The C-series aimed at measurements of selective transport processes. The series started again from a 1 in 40 sloped plane, in which the upper 10 cm of the bed consisted of a mixture of 60% sand and 40% Zircon by mass. During runs hydrodynamic parameters were recorded; in between the runs, profile and sediment composition were measured.

The objective of the D-series was to test a new device to record “friction” sound. These experiments were carried out with still water on the end profile of Series C.

The test conditions (see Section 2.3) and beach geometry were chosen according to test 1 of Roelvink and Stive (1989).

Table 2.1: Initial geometry, sediment composition (in mass percentages) and total duration of the various experiments

<i>Series</i>	<i>Initial geometry</i>	<i>Sediment</i>	<i>Total wave duration (hrs:min)</i>
A	plane, 1:40	Sand	28:27
B	end profile series A	Sand + Zircon placers	3:32
C	plane, 1:40	60% sand, 40% Zircon	14:33
D	end profile series C	60% sand, 40% Zircon	-

In Appendix B, an overview is given of the measurements carried out, the measuring positions per wave half-hour and the corresponding code names.

The instrumentation used in the respective series is described Section 2.5.

## Test procedures

*Series A* were subdivided in a number of "wave half-hours". During each wave half-hour, a *time-series* of exactly 35 minutes (the steering signal + 4.5 minutes) was generated, starting at the same position in the steering signal. To be able to compare the time-dependent measurements, the post-processing of these data will be done on the final part of the time-series with the length of the steering signal. The time-averaged suction system was operated during the last part of the time-series corresponding to the length of the steering signal. In series C, besides half-hour runs also hour runs were carried out in which during 65 minutes waves were generated. For these measurements, the analysed time-series will be twice the length of the steering signal. Also the suction system was operated during a period twice the steering signal. All instruments with time-dependent measurements were sampled simultaneously at 50 Hz. To avoid aliasing, a low-pass 25Hz analogue filter filtered each signal before storage.

At specific time intervals (mostly the end of the day) profile measurements were conducted by an automatic sounding system. As a standard procedure, measurements were made along two parallel trajectories, each running 33 cm from one of the side-walls of the flume. The profile data were stored at 0.04 m intervals and were stored on a separate PC. In addition, in some of the cases also the profile in the middle of the flume was measured. For selected profiles in the A-series and for all profiles in the C-series, the MEDUSA detector was attached to the profiler carriage. The MEDUSA logging PC was connected to the profile logging PC with an RS232 coupling for position information.

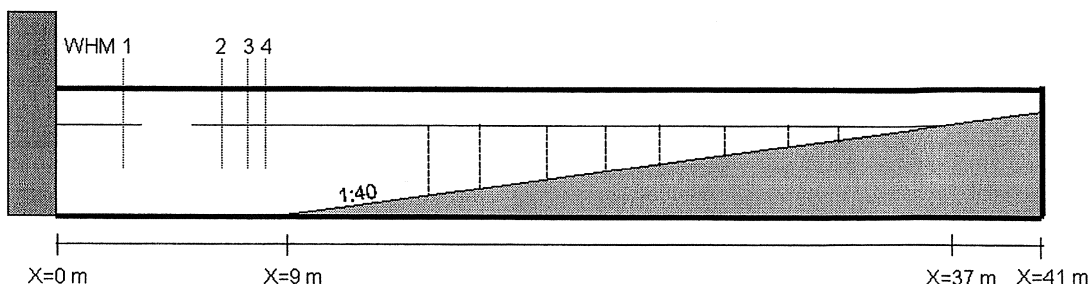


Figure 2.1 Schematic set-up of the experiment with co-ordinate system, locations of wave height meters (WHM) and positions of measuring verticals (vertical dashed lines). The grey box on the left-hand side of the figure shows the location of the wave paddle.

## 2.3 Steering and wave conditions

Random waves were generated by a wave board equipped with an active wave-absorption system (Klopman, 1995), such that at the same time waves were generated and reflected waves were absorbed. The latter prevented the re-reflection of free, long waves travelling offshore towards the wave board. The reflection compensation was operated such that waves with periods up to 60 seconds are completely absorbed by the wave board. Note that according to Dean and Dalrymple (1984) in the present set-up, a period of natural oscillation of  $1.642L/\sqrt{gh} = 50s$  is expected, with  $L=41m$  being the length from wave board to the maximum water line and  $h=0.7 m$  being the maximum water depth.

The waves were generated according to a second-order Stokes wave theory. This second-order wave board control includes corrections for the suppression of spurious free subharmonic and superharmonic components. The random wave fields generated were of the Jonswap type with a peak enhancement factor of approximately 3.3 representing a young sea state as expected under normal sea conditions. An improved method for wave generation (Klopman, 1998) was used which is closer to the theoretical second-order spectrum with respect to the energy content for frequencies larger than the peak frequency. The incident wave conditions at deep water (water depth  $h = 0.7 m$ ) and geometry are waveheight  $H_{m0} = 0.17 m$  and wave period  $T_p = 2 s$ . The wave-board control signal repeated itself every 1820.44 seconds.

## 2.4 Sediment

The sediment properties of the Quartz and Zircon used in series A-C are summarised in Table 2.2 and Figure 2.2. The grain-size distributions in Figure 2.2 shows that the Zircon is somewhat smaller than the Quartz ( $14 \mu m$  for the  $d_{50}$ ) but that the shape of the distribution is similar. The activity concentrations for  $^{238}U$  and  $^{232}Th$  in Table 2.2 clearly show the enhanced activity concentrations for the Zircon. The activity concentration of  $^{40}K$  is smaller than the minimum limit of detection which is high due to the high concentrations of  $^{238}U$  and  $^{232}Th$ . The results of the sample analysis imply that with the radiometric fingerprinting method as described in Venema *et al* (1999), the Zircon concentration in the sediment can be determined with an absolute accuracy of  $\sim 5\%$ .

Table 2.2 The grain size properties (in  $\mu\text{m}$ ) and activity concentrations (with external uncertainties) of  $^{40}\text{K}$ ,  $^{238}\text{U}$  and  $^{232}\text{Th}$  for Quartz and Zircon.

Sediment	$d_{10}$ ( $\mu\text{m}$ )	$d_{50}$ ( $\mu\text{m}$ )	$d_{90}$ ( $\mu\text{m}$ )	$^{40}\text{K}$ (Bq/kg)	$^{238}\text{U}$ (Bq/kg)	$^{232}\text{Th}$ (Bq/kg)
Quartz	93	129	187	6.8 (0.9)	5.6 (0.3)	4.82 (0.15)
Zircon	83	115	153	<580	12400 (400)	2300 (100)

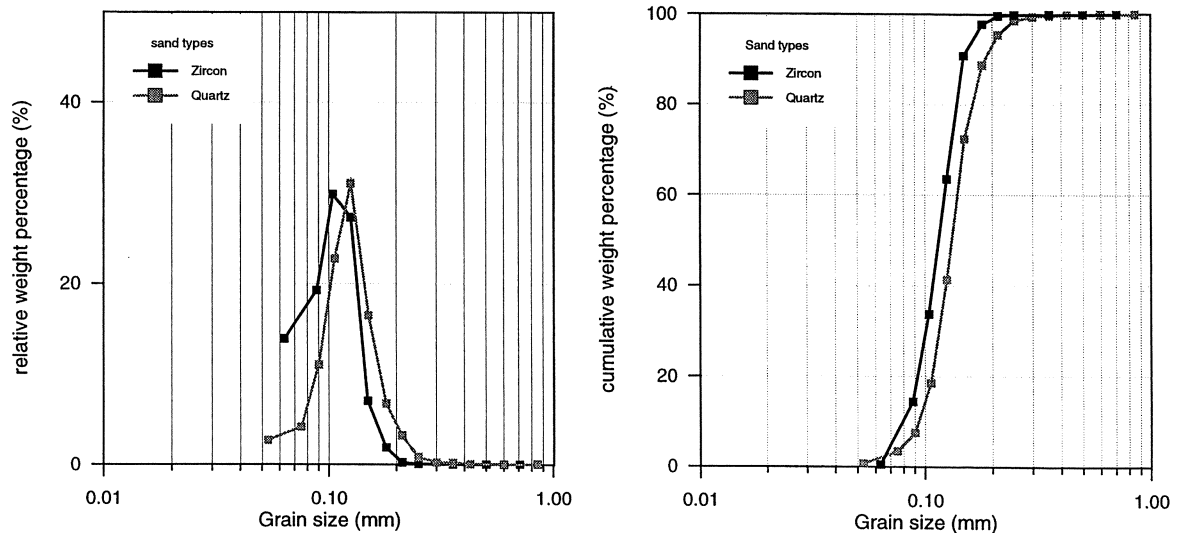


Figure 2.2 Relative and cumulative grain-size distributions for Quartz and Zircon

## 2.5 Instrumentation and data acquisition

### 2.5.1 General

Within the experiments, the instrumentation was adjusted to specific queries of each series. In this chapter the instrumentation and data acquisition are described. A more detailed description of the instruments that give time-averaged and time-dependent results and their calibration can be found in chapters 3 of data report part 1 and part 2, respectively.

Table 2.3 gives a general overview of the instruments that were used in each series. The time-dependent suspended sediment meter OpCon and the time-dependent velocity meter ADV on carriage 1 and carriage 2 are named OPC01 and ADV01 and OPC02 and ADV02, respectively.

Table 2.3 Overview of the use of the different ADVs, OPCONs, number of tubes of the transverse suction system that are used during the experiment, PROVO, MEDUSA, Wave height meters (WHM), settling tube and KVI in-house BGO detector

Series	ADV 01	ADV 02	OPC 01	OPC 02	# tubes	Provo	MEDUSA	WHM	Settling tube	BGO detector
A	*	*	*	*	4	*	*	6	*	
B						*	*			
C		*		*	8	*	*	5		*
D						*	*			

## 2.5.2 Measurements during runs

During the runs the following instruments were deployed for time-averaged measurements:

- Transverse suction system;

and for time-dependent measurements:

- Wave height meters (WHM);
- Optical concentration meter (OPCON);
- Acoustic Doppler Velocity meter (ADV) and
- video and photo camera.

Photographs and video recordings were made of ripple structures, ripple movement and experimental set up. Some of the photo's are used as illustration.

The free surface elevation, with respect to still water level was recorded continuously with wave height meters (WHM). Four resistance-type twin-wire WHM's were placed in the flume at the following locations (Table 2.4):

Table 2.4 Co-ordinates of the fixed and mobile wave height meters (WHM).

Code	x (m)	y (m)
WHM01	2.80	0.5
WHM02	6.56	0.5
WHM03	7.97	0.5
WHM04	8.44	0.5
WHM05	Carriage I	0.18
WHM06	Carriage II	0.21

The locations were chosen such that in principle the incoming bound, incoming free, the reflected free and reflected bound components may be separated. Besides the four wave gauges at a fixed position, two wave gauges were located on the measurement carriages.

## Measurement carriages

Most of the instruments operated during the runs were situated on a measurement carriage. Since the general objectives of the A and C series differ, special assemblies were used for each experiment.

During series A two measurement carriages (number 1 and 2) were used each equipped with:

- Transverse suction system (2 separate suction tubes at equal height but different y-location at each carriage)
- Acoustic Doppler Velocity meter (ADV)
- Optical Concentration Meter (Opcon)
- one resistance type wave gauge

During series C one measurement carriage (number 2) was used equipped with:

- Transverse suction system (8 suction tubes distributed in vertical direction)
- Acoustic Doppler Velocity meter (ADV)
- Optical Concentration Meter (Opcon)
- one resistance type wave gauge

Except for the ADV's, the instruments during the A-series on the both measurement carriages (Figure 2.3) were similar. For the carriages two different ADV's were employed. ADV01 refers to the ADV placed on carriage 1 and has a sampling volume located 0.10 m below the probe tip, whereas for ADV02 (located on carriage 2) the sampling volume is located 0.05 m below the probe tip. The smaller distance between sampling volume and probe tip for ADV02 means that the second carriage can be deployed up to lower water depths than carriage 1, consequently carriage 1 is located offshore of carriage 2 in case of simultaneous deployment (series A only). In the C-series, only carriage 2 is used.

The carriages were placed on wheels and can be moved along the x-axis of the flume. Moreover, the OpCon, ADV and suction tubes on the carriages are moved jointly in vertical direction to allow measurements at various locations above the bed. The wave height meters (WHM's) on the carriages are not connected to the other instruments and are kept to a fixed position with respect to the water level.

To determine the vertical positions of the instruments with respect to the sediment bed, the carriages were equipped with a 'depth-reference rod', a metal rod with on the lower end a PVC plate ('Peilvoetje') which can be rotated in the x-z plane (2<sup>nd</sup> left instrument in Figure 2.3). In this way it can be placed on the sloping sand bed over the rippled structures. Before each new run, this 'depth-reference rod' was placed on the sediment and with a marker on the metal rod, the instruments could be placed at 10cm above the sediment. By the use of a measuring rod attached to the carriages the relative position of the instruments with respect to the sediment could be adjusted. The uncertainty in the position of the instruments with respect to the bed (due to cross-flume morphologic variations and uncertainties the deployment the metal rod) is estimated as 0.5cm. These measurements were repeated after the experiments to determine bed-level variations.

The y-locations of the various instruments on the measurement carriages with respect to the glass wall on the w-side of the flume are given in Table 2.5 (see also Figure 2.3 which is a photograph of carriage 1 during series A).



Table 2.5 Locations of instruments on the carriages during series A and C.

y-locations (cm from w-side) of various instruments	Series A Carriage 1	Series A Carriage 2	Series C Carriage 2
WHM	18.2	21.1	21.1
Suction tube w-side	32.3	31.2	
OPC	49.2	47.8	47.8
'Peilvoetje'	62.5	59.5	59.5
ADV	75.5	73.0	73.0
Suction system			31.2
Suction tube d-side	93.5 <sup>1</sup>	92.8 <sup>2</sup>	

<sup>1</sup> 87.5 cm during series A1\* and A2\*

<sup>2</sup> 87.2 cm during series A1\* and A2\*

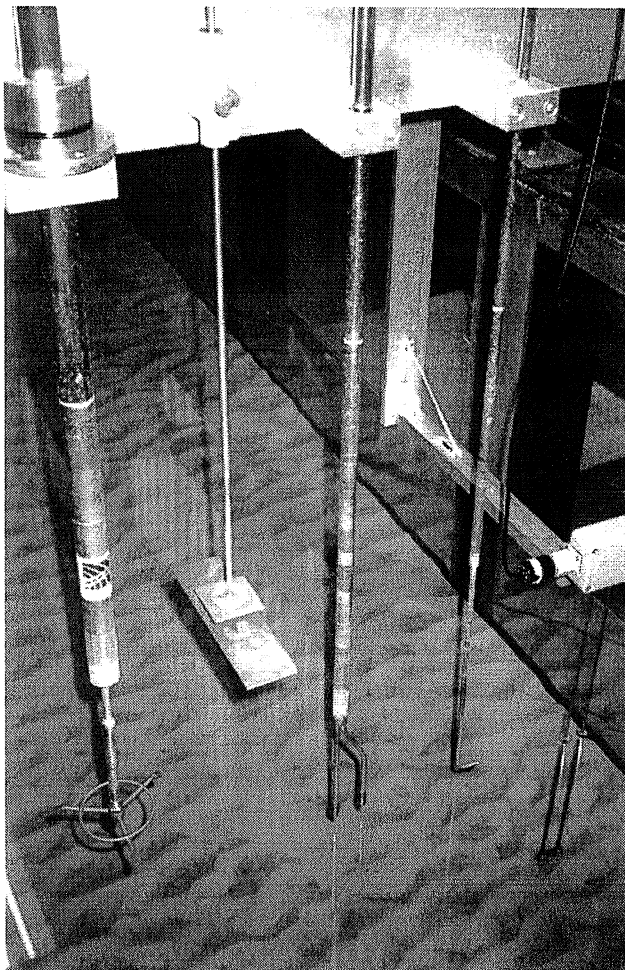


Figure 2.3 Measurement carriage 1 during the A-series, looking into the direction of the wave board. From left to right equipped with: suction tube d-side (not visible), ADV, depth-reference rod, OPCON, suction tube w-side and WHM.

The locations of the carriages in the different experiments is denoted in Table 1.2 and Table 1.3 in Appendix B.

### **2.5.3 Measurements between runs**

Between the runs, profile measurements (with the PROVO system) and measurements of sediment composition (with the MEDUSA system) were conducted. The PROVO is an automatic sounding system to measure bed height whilst the MEDUSA-system measures  $\gamma$ -ray spectra from the sediment and friction sound generated in the movement of the detector over the sediment. An elaborate description of both instruments can be found in chapter 3 of data report part I.

The locations of the carriages in the different experiments is denoted in Table 1.18-Table 1.20 in Appendix Appendix B.

### **2.5.4 Sample analysis**

Suspended sediment, collected in the transverse suction system during the A series, was analysed on grain size with a settling tube located at “de Voorst”. The collected sediments from the suction system in the C series and samples that were taken from the bed at the end of series C were analysed radiometrically on the Zircon concentration on a  $\gamma$ -ray detector located at KVI.

## 3 Instrumentation and calibration

### 3.1 PROVO

The bed-level profiling system (PROVO) consists of a bed profiler, a position counter (which determines the exact location of the profiler), and measuring and processing software. The profiler is placed on a carriage that can move with a maximum speed of 10 cm/s over the flume. The profiler, developed by WLIDELFT HYDRAULICS consists of a wheel connected to an aluminium rod by a highly sensitive spring. Whenever the pressure on the wheel changes (when it starts to move over a ripple structure for example) an electronic signal is sent by the spring to the carriage where the aluminium rod is moved up or down. A potential meter measures the vertical position of the rod.

The horizontal (x) position is calibrated once, at the beginning of the experimental programme. The (z) position is calibrated at the beginning of each set of profile measurements. By positioning the profiler at a location without sediment at  $y=0.67\text{m}$  and  $x=7\text{m}$  by using the position counter on the measuring PC. At this location, the profiler was set to the bottom of the flume and the zero level was adjusted. To test whether the electronic gain shifted, the electronic output of the profiler was measured at four different fixed heights above the bottom. This procedure was repeated after the first two days and showed a constant gain. The PROVO has an accuracy in z-direction of 0.5 mm.

Table 3.1: Towing velocities, number of profiles, remarks an MEDUSA measurements of series A, B and C. If no remarks are given, the profile measurements are done prior to the MEDUSA measurements.

Series	towing velocity ( $\text{ms}^{-1}$ )	number of profiles	remarks	MEDUSA
A100	0.10	2	profile measured after MEDUSA	+
A106	0.07	2	recalibration x-position	
A207	0.07	2		
A309	0.07	3	before profile water drained from the flume	
A407	0.07	2		
A607	0.07	3		
A707	0.07	3		
A904	904-m: 0.07 904-d/w: 0.03	3	d/w side simultaneous with MEDUSA	+(only d/w side)
B100	0.07	2	water drained from the flume, addition of placers	+
B101	0.07	2		+
B102	0.07	2		+
B103	0.07	2		+
B104	0.07	2		+
C100	0.07	2	new sediment	+
C101	0.07	2		+
C201	0.07	2		+
C302	0.07	3		+(only d/w side)

C402	0.07	2	+
C404	0.07	2	+

The profile was measured for at least two locations in the cross direction of the flume ( $y=0.33\text{m}$  and  $y=0.67\text{m}$ ). In a number of runs, the middle part of the flume ( $y=0.5\text{m}$ ) was profiled as well. For each cross profile, the PROVO was repositioned on the measuring carriage. Small holders for the PROVO are constructed on the carriage to enable accurate positioning. The profiles were recorded with a spatial resolution in the x-direction of 4 mm.

Initially, PROVO and MEDUSA data were collected simultaneously (Table 3.1). For a good spatial resolution of the radiometric measurements, the measurements with MEDUSA could only be conducted with a towing speed of 0.03m/s. In the PROVO measurement after run A100 the data acquisition system failed and the profile had to be measured again. However, the sledge of the MEDUSA system flattens the small ripple structures, and the measured small-scale variations in morphology for profile A100 will be reduced. To avoid these problems, it was decided to measure the profile and the  $\gamma$ -ray activity (MEDUSA) of series A, B and C separately.

All profiles of series A, B and C were measured at a speed of 0.07 m/s. Only the runs on the profile after experiment A100 were measured with a speed of 0.01 m/s, after experiment A904 the speed was 0.03 m/s.

### 3.2 MEDUSA

The MEDUSA system (de Meijer,1998) is used to measure activity concentrations of  $^{40}\text{K}$ ,  $^{232}\text{Th}$  and  $^{238}\text{U}$  of the sediment bed of series B and C. The MEDUSA system (Figure 3.1) consists of a highly sensitive gamma-ray detector, a water depth sensor, a microphone and accessory electronics to power the sensors and to amplify, digitise and transmit the signals to a computer. The detector system is connected to the computer by a coaxial cable. The  $\gamma$ -ray spectra and the information of the other sensors are transmitted to the data-logging PC where they are combined with position information from the PROVO data logging PC. The detectors and electronics are housed in two separate watertight casings with a length of ~30cm and an inner diameter of 6 cm.

The  $\gamma$ -rays are measured with a BGO (Bismuth Germanium Oxide) scintillation crystal. When the  $\gamma$ -rays penetrate the scintillation crystal, the energy of the photon is transmitted into a light pulse that is detected by a photomultiplier tube (PMT). The signals from the photomultiplier tube are amplified and stabilised in the electronics (Figure 3.1). These signals are stored as  $\gamma$ -ray spectra on the data-logging PC.

To guarantee a constant geometry, the detector housing was placed on the sediment. The casing with the detector was connected to an aluminum rod. This rod was connected to the PROVO carriage such that it could be moved over the profile. Both casings were placed on a PVC sledge to prevent sediment to pile up in front of the tubes (Figure 3.2).

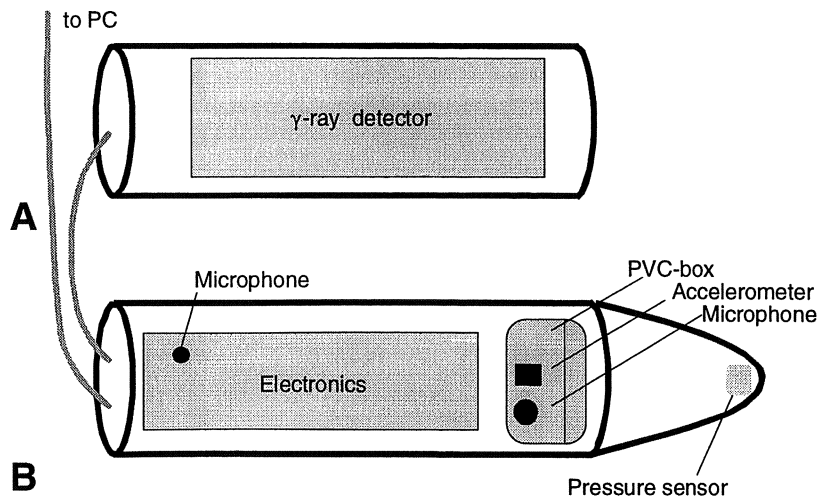


Figure 3.1 Schematic presentation of the MEDUSA set up for this experiment. The  $\gamma$ -ray detector is located in tube A, in tube B the electronics, pressure sensor and microphone are placed. The accelerometer and microphone that are used in series D are placed in tube B.

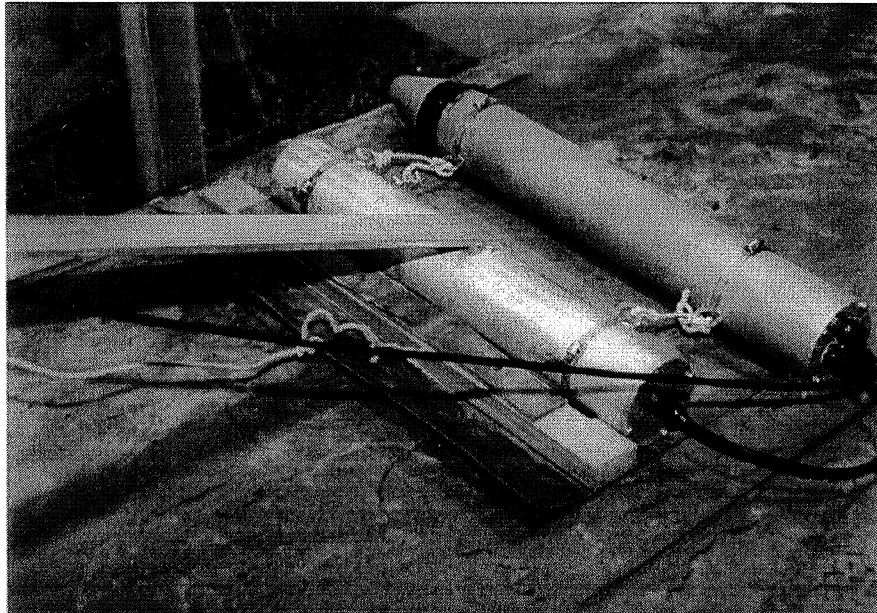


Figure 3.2: The MEDUSA set up in the flume. Tube A is located on the left side, tube B on the upper right side of the picture. The sledge is placed below both tubes to prevent sediment piling up in front of the detector.

Standard, the activity concentrations are calculated for a homogeneous, infinitely extending bed. However, for these experiments, attention is paid to the exact amount of transported Zircon and its concentration is calculated for a layer with a known thickness. These calculations imply that a model, that describes the relation between the measured activity and the concentration of Zircon in the bed, should be derived and calibrated. This model parameterisation and validation fall beyond the scope of the main body of the data report and are described in Appendix C.

### Coupling to x-position carriage

The MEDUSA system was connected to the PROVO data acquisition-system with an Rs232 cable. Via this connection, the x-positions of the PROVO-carriage were saved in the MEDUSA data files. With the information of the x and z-positions of the PROVO system, the exact x,z-positions of MEDUSA were calculated.

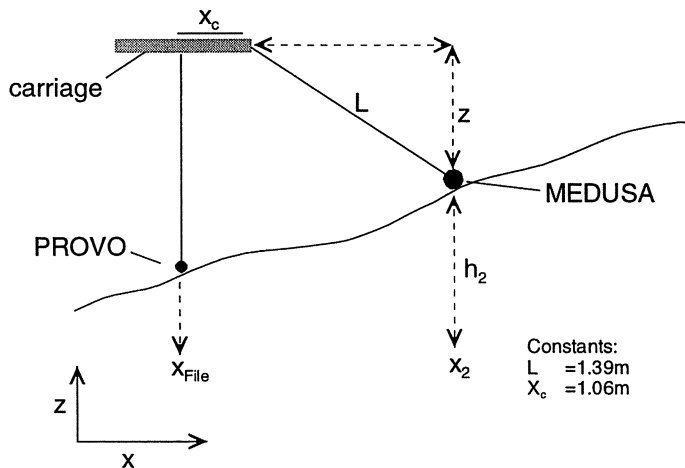


Figure 3.3: Schematisation of the MEDUSA and PROVO set-up.

In Figure 3.3, the set up is schematised. From the coupling between MEDUSA and the PROVO, the x-positions of the PROVO (here named  $x_{file}$ ) are coupled to the radiometric measurements of MEDUSA at position  $x_2$ . Since the relation between  $x_2$  and  $h_2$  are known (these data are stored in the PROVO data files), the stored position  $x_{file}$  is related to the exact location of MEDUSA ( $x_2$ ) via equation ( 3.1 )

$$x_{File} = x_2 - x_c - \sqrt{L^2 - z^2} . \quad ( 3.1 )$$

### 3.3 Transverse suction system

A transverse suction system was used to measure time-averaged suspended sediment concentrations at a height equal to the measuring volume of the OpCon. During series A two suction tubes were mounted on each carriage; each tube positioned on one side (Figure 2.3) of the carriage. During series C, 8 tubes were positioned at different (fixed) positions on the carriage. In Figure 3.4, the positions of the suction tubes for series C are schematically indicated. The tubes, with an inner diameter of 3 mm, were connected to pumps; the nozzle speed was of 1.2 m/s. The extracted volume of water is read from the volume scale on the buckets in which the water and sediment is collected. On average per suction tube two buckets were needed for 30 minutes of sampling. The extracted water returned to the flume.

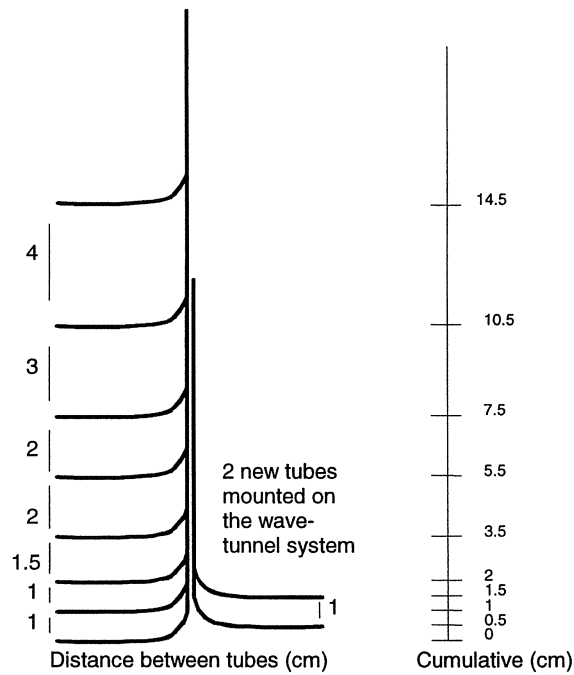


Figure 3.4 Layout of the suction system in series C

For series A, the mass of the suspended samples was determined via a volume meter, since this is faster than drying the samples and measuring on a balance. The suspended sediment samples were collected in a volume meter and artificially compacted by shaking the volumetric tube slightly. To derive the weight of the sediment from the measured volumes in these volumetric tubes, calibrations for different grain sizes are available. The grain size analysis of the suspended sediment samples (see section 3.4) gave values between  $66\mu\text{m}$  and  $120\mu\text{m}$ . The mass of the samples was determined from the calibration values of sand with a median grain size of  $112\mu\text{m}$ . For series C, the collected sediment is stored in plastic bags, dried in the oven at  $60^\circ\text{C}$  for 48 hours and weighed on a balance.

The transverse suction system is calibrated by the trapping efficiency  $\alpha$ , defined as the ratio of the sediment concentration in the sample over the concentration in the flow. The value of the trapping efficiency depends on the nozzle dimensions, their orientation relative to the flow, the ratio of the intake velocity over the ambient flow, the sediment particle characteristics and the relative density of the sediment (Bosman et al., 1987). According to Bosman et al. (1987), the intake velocity should be about three times the fluid velocity in a uni-directional flow to ensure a constant intake of sediment and constant trapping efficiency. In his paper however, Bosman writes that in measurements with oscillatory motions, the uncertainty caused by the variation in the relative intake velocity can be neglected due to the high random uncertainty caused by the volume measurements of the sampled sediment and the uncertainty in distance to the bed. Therefore, with peak velocities in the wave flume of  $0.6\text{ m/s}$ , the  $1.2\text{ m/s}$  water velocity in the nozzle is sufficient. The calibrations of Bosman indicated that the trapping efficiency  $\alpha$  for these sediments is in the range  $0.75\text{-}0.8$ , for the calibration of present experiments  $\alpha$  is set to  $0.77$ .

### 3.4 Settling tube

A settling tube located at “de Voorst” is used to determine the grain size of samples collected with the transverse suction system. The settling tube has a length of about 2m and the lowest part consists of a measuring-cylinder. A teaspoon of sediment is released from the top of the tube and at constant time intervals, the settled volume is measured. Since the length of the tube is known, the mean fall velocity of the sediment can be calculated. From these fall velocities, the grain size is determined, applying the empirical equations of Van Rijn (1990) for non-spherical particles:

$$w_s = \frac{\Delta g d^2}{18\nu} \quad \text{for } 1\mu\text{m} < d \leq 100\mu\text{m} \quad (3.2)$$

$$w_s = \frac{10\nu}{d} \left( \sqrt{1 + \frac{0.01\Delta g d^3}{\nu^2}} - 1 \right) \quad \text{for } 100\mu\text{m} < d \leq 1000\mu\text{m} \quad (3.3)$$

Where:

$w_s$  = settling velocity ( $\text{m s}^{-1}$ )

$g$  = gravity acceleration ( $\text{m s}^{-2}$ )

$d$  = grain diameter (m)

$\nu$  = kinematic viscosity coefficient ( $\text{m}^2\text{s}^{-1}$ )

$$\Delta = \frac{\rho_s - \rho_w}{\rho_w} \quad (-)$$

$\rho_s$  = density of sediment ( $\text{kg m}^{-3}$ )

$\rho_w$  = density of water ( $\text{kg m}^{-3}$ )

### 3.5 BGO detector sample analyses (laboratory)

The concentrations of Zircon in the sediment samples that were taken at the end of the B and C-series and in the samples from the suction system of series C, are derived from the  $\gamma$ -ray activity measured on the in-house Bismuth Germanate ( $\text{Bi}_9\text{Ge}_3\text{O}_{12}$ ) or BGO crystal at KVI. BGO crystal is surrounded by 10cm of old lead to reduce the background radiation from building materials. The remaining background signal is mainly the result of cosmic radiation and by radioactive  $^{214}\text{Bi}$ -nuclei in the crystal itself.

The aim of the measurements of the sediment samples was to determine the concentration of Zircon. Similarly to the measurements with the MEDUSA system (Appendix C), total count rates of the  $\gamma$ -ray spectrum are recorded. With the differences in total count rate between Zircon and Quartz, the Zircon concentration in the measured samples were derived.

By using the total count rates of the major part of the spectrum, the Zircon concentrations of the samples could be measured fast (100s per sample) with inaccuracies in the Zircon content <10% (relative uncertainty).



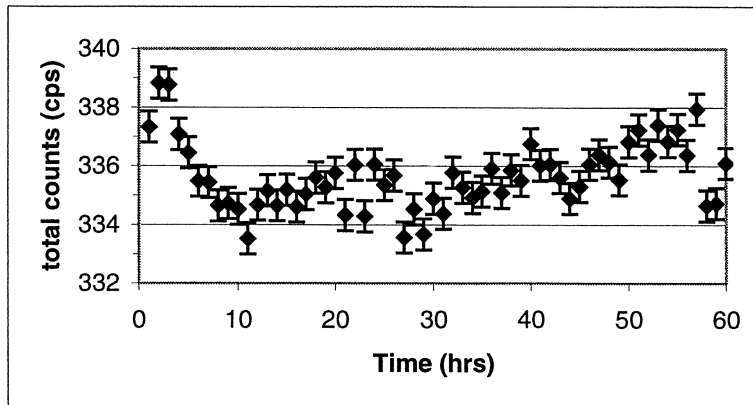


Figure 3.5: Variation in count rate over 60 hours.

### Calibration detector set-up

The total count rate was measured in a region of interest (ROI) covering the energy range  $0.45 \text{ MeV} < E_{\gamma} < 4.5 \text{ MeV}$ , set for all measurements. Background was measured overnight. To determine absolute values, the spectrum of the  $\gamma$ -ray detector must be stabilised. In the field measurements with the MEDUSA system, the absolute energies of the spectrum change mainly by variations in temperature. For these measurements, the spectrum is stabilised continuously by the logging and data-analysis software. Since the external variations in the present set-up in the laboratory are small, it is assumed that the detector is stable and that the absolute position of the  $\gamma$ -ray spectrum does not change much. To determine a possible drifting of the detector, the activity concentration of a source (a box with constant amount of Zircon) was measured in intervals of 1200s for two days (Figure 3.5). These data show that the gain of the detector shows a variation which can probably be described to changes in temperature during day and night resulting in variations in count rate of maximum  $6 \text{ count s}^{-1}$ . However, this variation is small ( $\sim 1\%$  (relative)) and since the samples are measured for a smaller sampling period, this 1% inaccuracy due to a drifting of the detector is much smaller than the statistical uncertainty. Therefore, the drifting of the detector system is neglected and the calibration measurements are conducted once, at the beginning of the measurements.

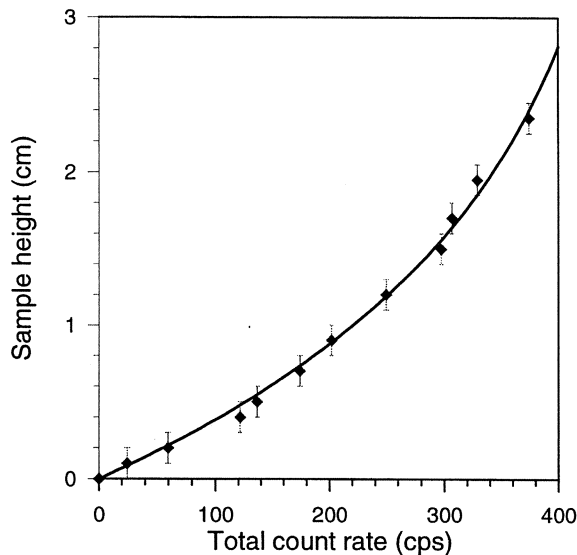


Figure 3.6: Calibration measurements with the activity sample height as function of total count rate. The line represents the fit given in equation ( 3.4 )

The sediment samples were put in small pillar-boxes with a maximum volume of 60 ml and were placed on top of the detector . To determine the relation between the amount of Zircon (height in the box) and count rate, measurements with varying thickness of Zircon were conducted (Figure 3.6). The uncertainties in activity concentrations of Zircon in Figure 3.6, are pure statistical uncertainties and fall within the size of the data points. The uncertainties in sample height are due to the height measuring technique. To determine the height, a ruler is set to the side of the box, and the height is read by eye. An inaccuracy of 1mm is estimated as uncertainty of this procedure.

To parameterise the relation between height and count rate, it is assumed that the increased count rate due to increasing sediment thickness is reduced by self absorption of the sediment (see Appendix C) and that the measurements can be fitted according to equation ( 3.4 )

$$N(z) = \frac{L\varepsilon}{\mu'\rho} (1 - e^{-\mu'\rho z}) . \quad (3.4)$$

where L is the specific count rate of the sediment (in counts per second per layer sediment thickness),  $\varepsilon$  accounts for detector efficiency and geometry, z the thickness within the pillar-box and  $\mu'\rho$  the mass attenuation coefficient times the density for Zircon in this geometry.

In a  $\chi^2_{\text{red}}$  (see Appendix D) fit procedure, only the uncertainties in the dependent (y) variable are accounted for. Since the uncertainties in the height of the samples are much larger than the statistical uncertainties in the count rate, the determination of the fit parameters with equation ( 3.4 ), would result in an overestimation of  $\chi^2_{\text{red}}$ . Therefore,  $\mu'\rho$  and L are determined by the inverted function of equation ( 3.4 ). This allowed to determine a proper  $\chi^2_{\text{red}}$ . The resulting fitparameters, their uncertainties and the quality of the fit are printed in Table 3.2 .

Table 3.2: Fit parameters and  $\chi^2$  for the calibration curve of Zircon. Uncertainties are given within brackets

	$L\mathcal{E}$ ( $s^{-1} cm^{-1}$ )	$\mu'\rho$ ( $cm^{-1}$ )	$\chi^2_{red}$
Zircon	293 (10)	0.59 (0.04)	0.4
Quartz	0.52 (0.05)	0.39 (0.09)	1.1

The measured count rate of a box of sediment will be a function of the thickness in the box,  $\mu'\rho$  and  $L\mathcal{E}$  (equation ( 3.4 )). In a sediment mixture, the parameters  $\mu'\rho$  and  $L\mathcal{E}$  of the mixture will be the sum of the weight fractions ( $w_i$ ) of element  $i$  times the parameters  $\mu\rho_i$  and  $L\mathcal{E}_i$  of each element (equation ( 3.5 )).

$$\begin{aligned}\mu'_{mixture} &= \sum_i w_i \mu'_i \\ L\mathcal{E}_{mixture} &= \sum_i w_i L\mathcal{E}_i\end{aligned}\quad (3.5)$$

The measurements of pure Quartz samples showed that the count rate of a full box of Quartz was only  $0.8 s^{-1}$ . Since the activity of Zircon is an order of magnitude larger than that of Quartz (even 1mm of Zircon (which is the smallest sample that can be measured) gives 28 counts  $s^{-1}$ ), the contribution of Quartz in the count rate of Quartz is neglected. This implies that for a given thickness, the count rate of a sediment mixture would be linearly related to the concentration of Zircon in the mixture. To determine whether neglecting Quartz in the calculation of the sediment composition is valid, the relation between Zircon content and count rate is calculated with equation ( 3.4 ) by calculating an  $\mu'\rho_{mixture}$  and  $L\mathcal{E}_{mixture}$  (Figure 3.7). The linear regression trough the datapoints of Figure 3.7 with an  $r^2=0.99$  shows that the relation between the count rate and Zircon concentration is linear. Therefore, the concentration of Zircon is determined from the ratio (equation ( 3.6 )) of the measured count rate of the sample and the expected count rate for an equal amount of Zircon that can be calculated with equation ( 3.4 ). Since activity concentrations  $<0.8$  cps probably result from variations in composition of the Quartz minerals, the Zircon concentrations of these data points are set to 0.

$$m_{zircon} = \frac{N_{measured}}{N_{100\% zircon}}\quad (3.6)$$

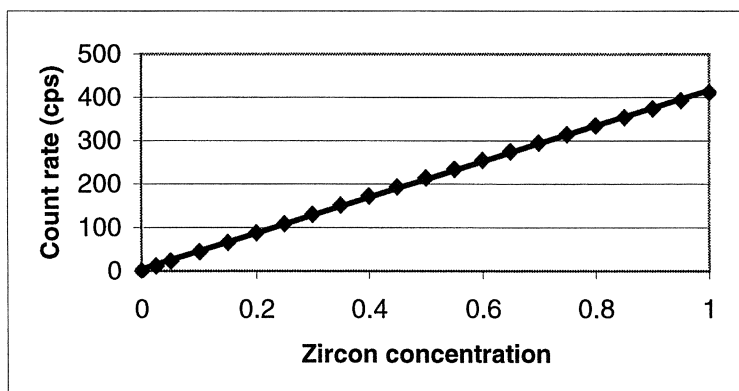


Figure 3.7: Calculated relation between count rate (equation ( 3.4 )) and Zircon concentration. The linear regression trough the data points has an  $r^2=0.99$ .

The uncertainty estimations of the Zircon concentrations of the samples follow from the error propagation of two sources: the statistical uncertainty in the count rate and the uncertainty in the determination of the bed height (set to 1mm). The relative error due to the bed height will be largest for small samples and it is not possible to improve this part of the uncertainty. Increasing the measuring time can solve the inaccuracy due to poor statistics in the count rate. For most of the samples, a measuring time of 100 s is used. However, since increasing the measuring time (up to a maximum of 600 s) could increase the accuracy of the result, extra measurements were conducted for samples with too low counting statistics.

To get an impression of the quality of the results of the method, test samples are measured. Four samples, varying in height but with a mass-percentage of  $0.5000 \pm 0.0006$  of Zircon were measured to determine their Zircon content. The averaged measured Zircon concentration of these samples is  $0.48 \pm 0.01$ , while the external uncertainty (the standard deviation in the data points) is 0.017. This analysis shows that the radiometric determination of the Zircon concentrations in the samples and the error estimation can be done accurately.

## 4 Data analysis and validation

### 4.1 Bed heights and sediment transport rates

The quality of the profile measurements was checked by a manual search for outliers and spikes. These checks and the visualisation of the profile changes for series A and C in Figure 4.1 and Figure 4.2 respectively, show that the profile look plausible.

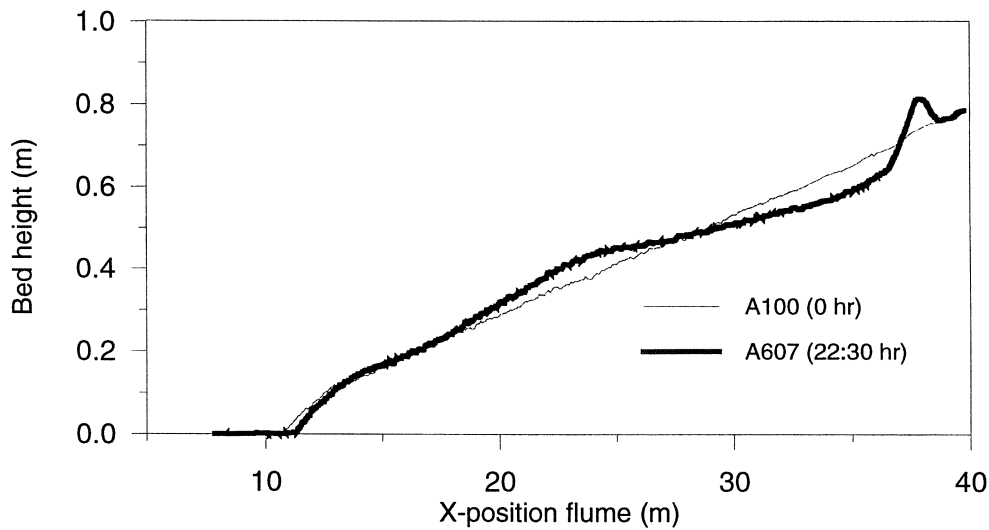


Figure 4.1: Profile change for the A-series experiments

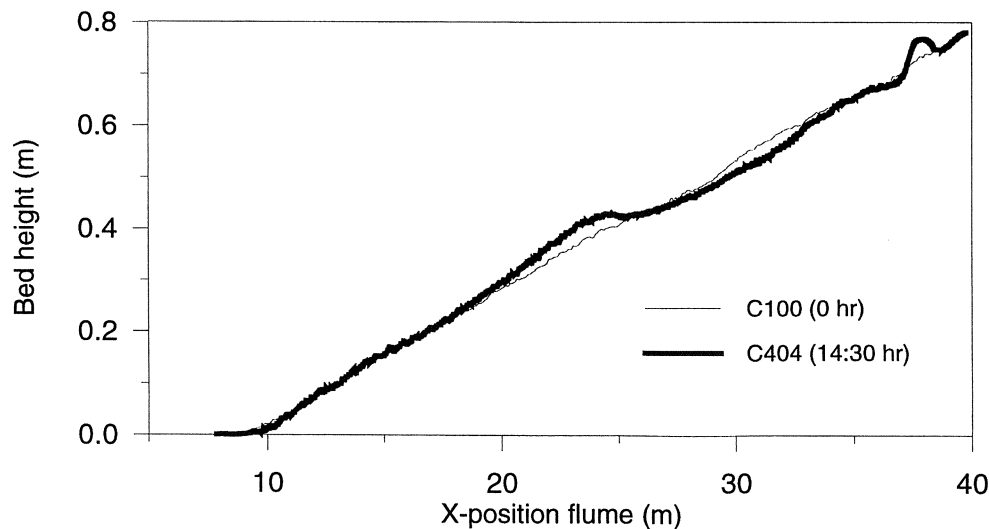


Figure 4.2: Profile change for the C-series experiments

The morphology of the bed profile is the direct result of sediment transport, and can be parameterised in variations in profile height  $\Delta z$ , inferred from subsequent profile measurements. Where the variations in height give information on profile change, sediment transport rates describe the direction of sediment movement. The variations in height can be used to formulate a volume balance to determine the time averaged sediment flux or transport rate  $\langle q \rangle$  per unit width ( $W$ ), in  $\text{m}^3 \text{m}^{-1} \text{s}^{-1}$  in a cross section on location ( $x$ ):

$$\langle q(x) \rangle = \frac{1}{W\Delta t} \int_{\text{offshore}}^{\text{beach}} -\Delta z(x) dx, \quad (4.1)$$

with  $\Delta t$  the time variations between the different profile measurements. If the total volume in the section of study is constant, the calculation of the integral from offshore to beach should yield the same results as the calculation from beach to offshore.

The principle in the determination of the volumetric sediment transport calculations is based on the assumption that the total volume of sediment in the flume is conserved and the total volume variation should be equal to 0. In the set up of the experiment, special attention was paid to the initial porosity of the sediment bed. The profile was built underwater such that the enclosure of air bubbles in the sediment could be avoided. After the profile was built, the water was let out several times and the sediment was compacted by walking through the wetted flume. For the A-series, small high frequency waves were used to further compact the sediment underwater, for the C-series this was not possible, because this would initiate selective transport of sediments.

To determine the assumption of a constant volume is correct, the volume in the flume that would have been inferred from each profile measurement (the integral of the variations in bed height) is calculated and plotted in Figure 4.3. The variations in volume measured on the different sides of the flume can be the result of the fact that the PROVO carriage is not exactly horizontal, but since only relative changes for each profile transect are used, this will not lead to erroneous results. The variations in volume show that changes of sediment of 20 L between two profiles occur. This can be caused by various mechanisms:

- 1) The total volume of sediment is not conserved due to removal of sand from the flume.  
If 20 L of sediment were drained from the flume, this would have been observed at the stretch of flume without sediments near the wave paddle. Moreover, this effect will result in a constant decrease in volume, which is not the case, since for some profiles the total volume increases.
- 2) The porosity changes.  
Similar to the effect of loss of sediment, a change in porosity will result in a constant decrease in volume, which is not the case.
- 3) The cross flume profile changes and the 3 profilers (PROVO) are not descriptive of the total volume in the flume.  
The changes of the sediment bed in cross-flume direction will probably vary throughout the entire flume. This means that they might cancel. When variations in cross-bed direction occur, this effect will probably vary for the three profilers. The results in Figure 4.3 indicate that the general trend for the 3 profiles is similar, especially for the measurements of series C. For series A, the variations seem to be larger for the w-side. These results suggest that the large-scale fluctuations are not caused by variations in cross flume direction. However, the small-scale variations in cross-flume direction do influence

the profile measurement, and will have an effect on sediment transport rates. These effects will be assessed later.

- 4) The x-calibration of the PROVO is not constant  
The x-calibration was done twice, before run A100 and, by accident, before run A106 but was kept constant afterwards. Therefore, variations in the x-calibration can, except for profile A100, not account for the changes in volume.
- 5) The z-calibration of the PROVO is not constant.  
Before the profiling of each new run, the z-position of the PROVO system was recalibrated. This calibration can have an uncertainty of  $\pm 0.5$  mm. A systematic difference of 0.5 mm between two profiles will lead to a difference in total volume of 20 L. This value is in the range for the fluctuations on the total volume of sediment in the flume and the uncertainty in the z-calibration probably accounts for the changes in total volume.

The offset value between run C302\_C402 is larger than the 20 L that can not be the result of the statistical uncertainty in the calibration of the PROVO. This large difference is not understood and profile C402 is omitted from further morphological data analysis.

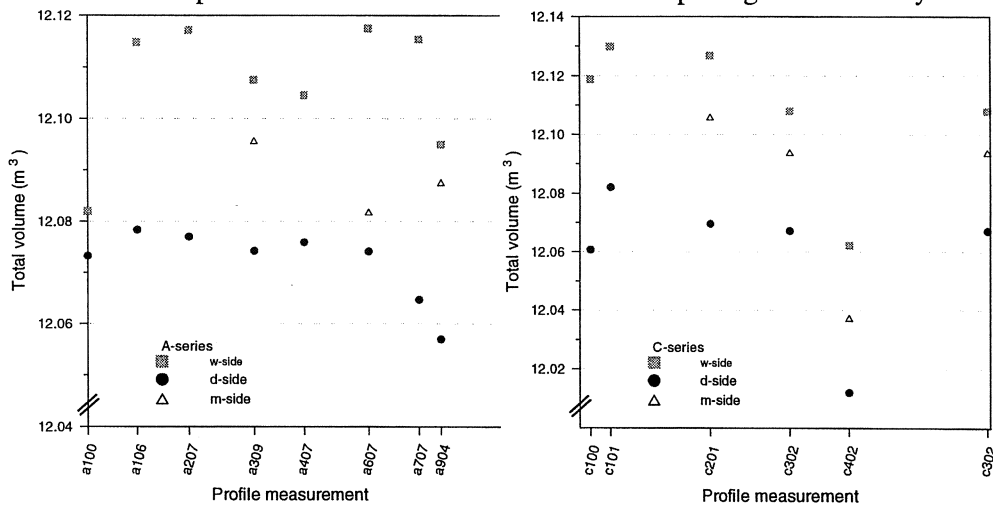


Figure 4.3: Total volume in the flume for each experiment of series A and C, measured with three different profilers. Statistical uncertainties of the PROVO fall within the data points.

If the total measured volume in the flume is constant, the total transport rate at  $x=39$  m (the maximum x-position of the profile measurements) should be 0. However, due to the offsets in the z-direction, described in previously, this is not always the case. Therefore equation (4.2) was adjusted by accounting for offset in the z-direction ( $z_{\text{offset}}$ ) due to errors in the calibration of the PROVO system:

$$\langle q(x) \rangle = -\frac{1}{W\Delta t} \int_{\text{offshore}}^{\text{beach}} (\Delta z(x) + z_{\text{offset}}) dx, \quad (4.2)$$

where values of  $z_{\text{offset}}$  are presented in Table 4.1.

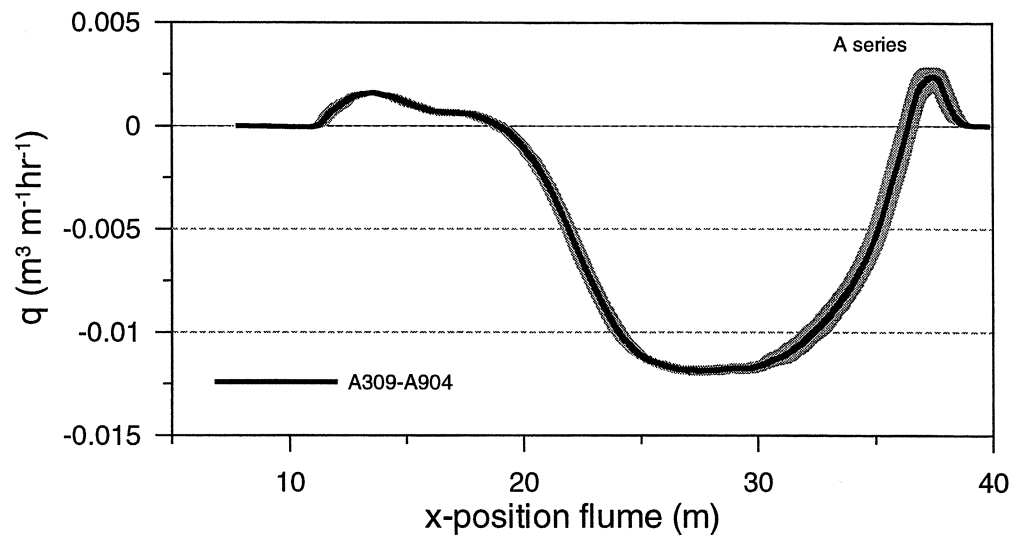


Figure 4.4: Sediment transport rates between profile A309 and A904. The grey line represents the standard deviation in sediment transport rate due to cross-flume variations.

The remaining uncertainty of variations in morphology in cross-flume direction on the transport rates can be determined from the standard deviation in the transport rates when three profiles were measured after a run. This standard deviation is measured for the two profiles of A607 and A707 Figure 4.4. These results show that the effect of variations in cross-flume direction are small.

Table 4.1: The net difference in mean height of the total bed per PROVO measurement step for series A and C.

name	offset W-side (mm)	offset D-side (mm)
A100_106	1.03	0.16
A106_207	0.07	-0.04
A207_309	-0.30	-0.09
A309_407	-0.10	0.05
A407_607	0.41	-0.06
A607_707	-0.07	-0.30
A707_904	-0.64	-0.24
C100_101	0.28	0.53
C101_201	-0.07	-0.31
C201_302	-0.48	-0.06
C302_402	-1.14	-1.38
C402_404	-1.55	-2.02



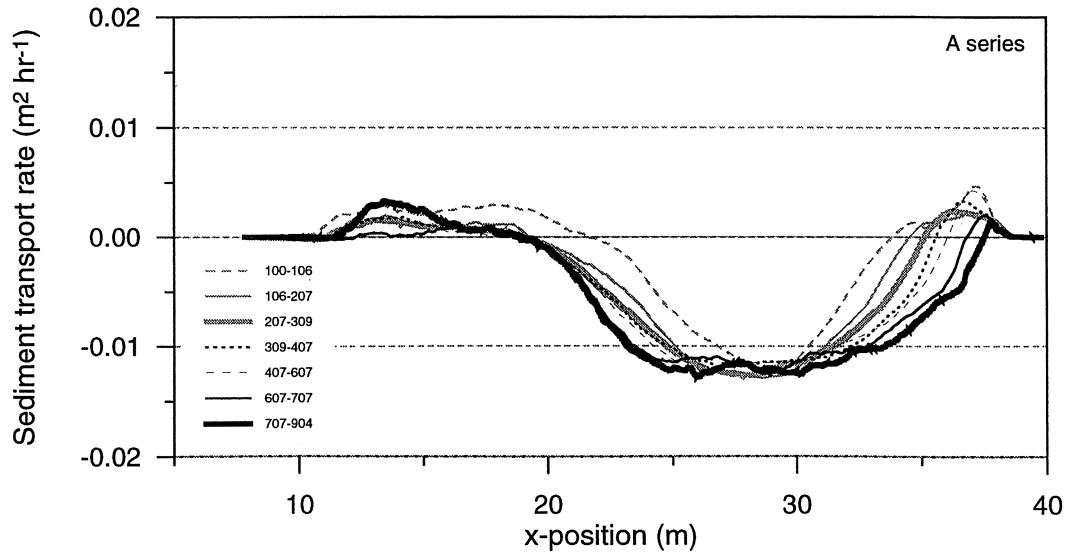


Figure 4.5: Sediment transport rates for successive profiles for series A.

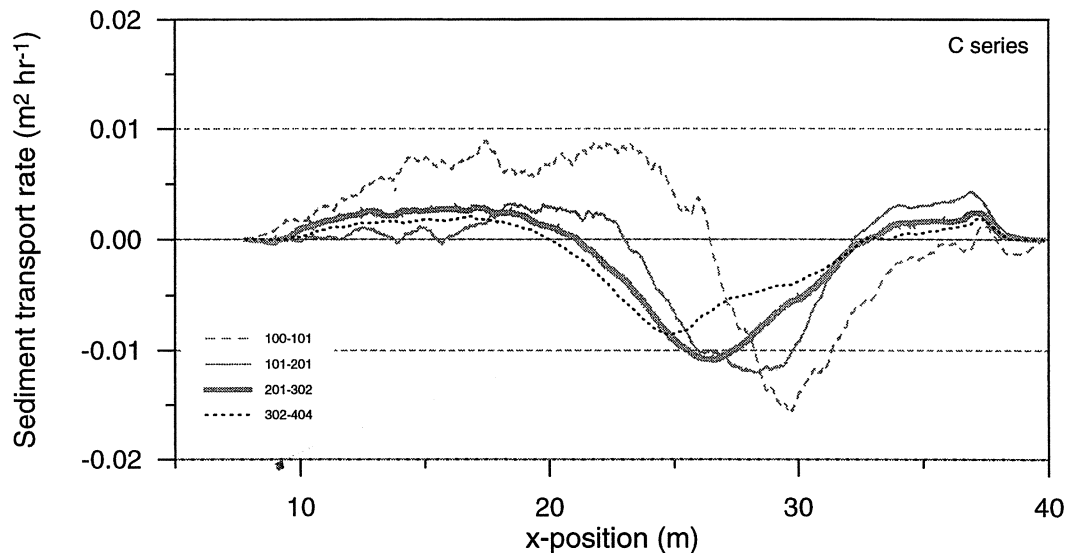


Figure 4.6: Sediment transport rates for successive profiles for series C.

Sediment transport rates for series A and C are presented in Figure 4.5 and Figure 4.6, note that although the transport rates are normalised on time, the time intervals between the different profile measurements differ (see Table 1.18 and Table 1.20 in Appendix B). It was expected that the profile would evolve towards equilibrium after a period of time and that transport rates would decrease and that transport gradients would move to 0, similar to other laboratory experiments (see e.g. Newe *et al*, 1999). However, the results of the transport calculations show that the transport rates of series A are getting larger until the end of the experiment in the regions between  $x=20-25$  m and between  $x=30-40$  m. In the region between  $x=25$  and  $30$  m, transport rates do not change but remain large. For series C, transport rates between  $x=20$  and  $x=25$  m, increase in time, whilst the transport rates between  $x=24$  and  $x=37$  m show a continuous decrease and even reverse sign between  $x=32-37$  m.

Where the transport rates of series A do not show a decrease in time, the transport rates of series C shows much more variation. For series A, transport rates remain large, but the transport gradients for  $25 < x < 35$  m become small.

Although the continuous evolving profile of series A was not expected, this indicates that the instantaneous measured sediment transport rates from the OPCON and ADV can be compared for each time period.

## 4.2 Mean concentration

For the A-series, suspended sediment concentrations were measured simultaneously with the transverse suction system (see section 3.3) at the two sides of the flume (d-side ( $y \sim 0.93\text{m}$ ) and w-side ( $y \sim 0.32\text{m}$ )). The correlation between the concentrations of both sides gives an estimate of the variation in the measurements (Figure 4.7).

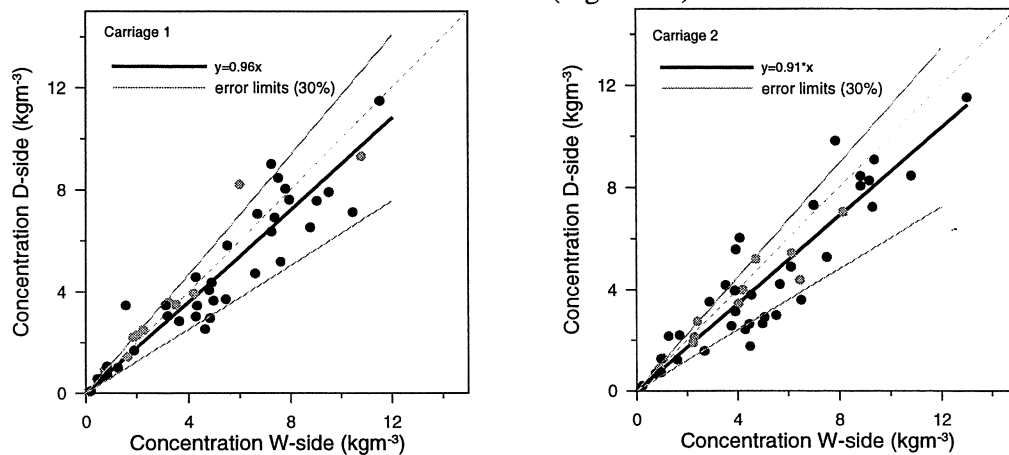


Figure 4.7: Correlation between sediment concentrations from D and W-side for Carriage 1 and 2, with the results of the fit  $y=ax$ . The dotted lines represent the line  $y=x$ . The grey dots present the measurements with the D-side tubes faced towards the centre of the flume, the black dots represent the measurements with the D-side tubes faced towards the wall of the flume.

A linear fit for both series shows that the concentrations from the tubes on the w-side are larger than the concentrations from the d-side tubes. The suction tubes on the w-side of the flume were located more in the middle of the flume, whilst the d-side tubes were located more to the walls of the flume. If any side wall effects would have occurred during the experiments, this effect will be most pronounced in the d-side results and would result in a reduction in the suspended sediment concentrations. The relation between the results of the d and w-side concentrations can be explained by this effect. In the analysis, the d-side results will be adjusted by a factor of 1.11 and 1.16 for carriage 1 and 2 respectively. Initially, the nozzles of the tubes on both carriages faced the centre of the flume and faced the ADV (grey dots in Figure 4.7). Since it was not clear if this had any effect on the measured velocity signal, the nozzles were turned such that the openings of the nozzles faced the wall of the flume (black dots in Figure 4.7). The data before and after turning the nozzle show that the influence of the facing direction of the tube on the suspended sediment concentration is negligible.

The spread of the measured concentrations around the linear best fit (Figure 4.7) was used to calculate the standard deviation. Similar to the findings of Bosman (1987), the error in the measured concentration is relative and has a value of 30%. Figure 4.7 shows the Uncertainty around the best fit of the data points.

Figure 1.1 and Figure 1.2 in Appendix A show the time-averaged suspended sediment concentration profiles from the suction system for various x-positions. For both series, these figures show a general trend of the decreasing sediment concentrations with increasing distance to the bed. In general, no major outliers are present.

## 4.3 Grain-properties

### Grain-size

The samples collected from the transverse suction system from the A series were analysed in the settling tube to give information on:

- $w_{10}$  : fall velocity not exceeded by 10% of sample volume
- $w_{50}$  : fall velocity not exceeded by 50% of sample volume
- $w_{90}$  : fall velocity not exceeded by 90% of sample volume
- $d_{10}$  : grain diameter not exceeded by 10 % of sample volume
- $d_{50}$  : grain diameter not exceeded by 50 % of sample volume
- $d_{90}$  : grain diameter not exceeded by 90 % of sample volume

Since the settling tube analysis procedure was time consuming, only the sediments collected in the w-side tube were analyzed. To estimate the variance in the grain size from samples from the d and w side, samples from 23 locations were analyzed in duplo (d and w side). These data were used to determine the variance in the data and determine the uncertainty in the grain size distribution. This uncertainty is estimated as 2  $\mu\text{m}$ .

Also the sediments collected in series A70#, A80# and A90# were only partly analyzed. Since these measurements included repeated measurements at one location, a grain size similar to that of the previous measurements was assumed.

Figure 1.3 in Appendix A shows the  $d_{50}$  grain-size profiles for various x-positions. The general picture shows that only the finest part of the sediments is brought into suspension, with a trend of decreasing  $d_{50}$  with increasing distance from the bed, also observed in other experiments. The data points seem to be consistent without any obvious outliers.

### Density

The samples that were collected from the transverse suction system in series C were analysed on their Zircon concentration with the BGO-detector. Figure 1.4 in Appendix A shows the Zircon concentration profiles for various x-positions. It appears that uncertainties are very large for some data points with Zircon concentrations close to 0. These uncertainties are mainly due to inaccuracies in determination of the volume of the very small samples. Since the uncertainty in the volume estimation is absolute, the uncertainties in small volumes can be relatively very large. A minimum limit of detection is adopted of 1%. Therefore, data points with Zircon concentrations smaller than 1% are presented as 0% Zircon concentration. The general trend for the zircon concentration over height is similar to that of the grain size of the sediment: the concentration of zircon decreases with height.

## 4.4 Sediment composition

The radiometric signal is converted to Zircon concentrations by the Full Spectrum Analysis (FSA) method (de Meijer *et al*, 1997) described in Appendix C. This spectrum deconvolution calculates the contribution of “standard spectra” of Quartz and Zircon to the measured  $E_\gamma$  spectrum. This spectrum deconvolution is done with the MPA (MEDUSA Post Analysis) software package. The accuracy of the fit results, which is purely based on the statistics of the fitted spectrum, was 0.1% absolute. These results are used to calculate the Zircon concentrations in the upper layer of the sediment by a simplified model described in Appendix C. The effective parameters of this model are determined with calibration measurements that were conducted in the flume in the geometry of the experiments. As an extra step in the validation of the calibrated model, results from sample analyses are compared to the results from the radiometric surveys. This step showed that by adjusting one of the three effective parameters (to a physically meaningful value), the sediment composition could be described within an accuracy of 5% (absolute) (for more details see Appendix C).

### Position accuracy MEDUSA measurements

The x-positions of the MEDUSA signal are calculated with the PROVO measurements. The x-positions from the PROVO carriage were sent to the MEDUSA data acquisition PC by an RS232 connection. In general this system worked properly, but in some cases the connection between carriage and MEDUSA PC failed after a period of time. Table 4.2 shows the MEDUSA filenames, the corresponding profile and position in the flume. A star and the location along the profile where the coupling failed denote the failed couplings. In the data files with failed couplings, the missing x,z data are substituted from the corresponding parallel profile by using the depth information provided by the MEDUSA water-pressure sensor.

Table 4.2: Overview of files, profile number and position in y-direction and coupling information

Filename	Profile and position	Coupling failed
SafeC100	C100-d	
SafeC110	C100-w	
SafeC101	C101-d	
SafeC111	C101-w	
SafeC201	C201-d	
SafeC211	C201-w	
SafeC302	C302-d	
SafeC312	C302-w	
SafeC402	C402-d	
SafeC412	C402-w	*(19-9 m)
SafeC404	C404-d	* (11-9 m)
SafeC414	C404-w	*(30-28 m)

The ADC converter of the MEDUSA data processing electronics malfunctioned in the experiments, which resulted in spikes at every 32<sup>th</sup> channel of the  $E_\gamma$ -ray spectrum. These spikes are removed from the signal by replacing the signal of each 32<sup>th</sup> channel with the average from the 31<sup>th</sup> and 33<sup>th</sup> channels.

## 4.5 Sound

The experiments of the D-series focussed on the relation between measured friction-sound levels and grain size. Figure 1.5 in Appendix B shows that the measurements of the normal MEDUSA sound levels are consistent between various measurements and indicates that uncertainties due to morphological variations in the sediment bed or set-up between measurements are negligible.

## 5 Conclusions and recommendations

The data presented in this report were obtained and analysed within the framework of the EU-sponsored MAST-III SAFE project. The measurements of hydrodynamics, suspended sediment concentrations, sediment transport and radiometry were carried out on a natural 2DV beach under erosive conditions in WL|DELFT HYDRAULICS' Scheldt flume. Besides dune sand (series A), also various mixtures of dune sand and heavy minerals were used to investigate selective transport phenomena of minerals with a different density (series B through D). Time-mean sediment concentrations, radiometry (bed composition), bed profile evolution (data report part I: Time-averaged measurements (Koomans and Bosboom, 1999) and time-dependent measurements (surface elevations and time-dependent velocities and sediment concentrations at one elevation above the bed; data report part II: Time-dependent measurements (Bosboom and Koomans, 1999) were measured for all mixtures.

Random waves were generated by a wave board equipped with an active wave absorption system (Klopman, 1995), such that at the same time waves were generated and reflected waves were absorbed. The latter prevented the re-reflection of free, long waves travelling offshore towards the wave board. The incident wave conditions at deep water (water depth  $h = 0.7$  m) and geometry are  $H_{m0} = 0.17$  m and a peak period  $T_p = 2$  s.

The following instruments were deployed for time-averaged and time-dependent measurements: transverse suction system, wave height meters (WHM), Optical concentration meter (OPC), Acoustic Doppler Velocity meter (ADV). Most of the instruments that were operated during the runs were situated on a measurement carriage. Since the general objectives of the A and C series differed, special assemblies were used for each experiment.

The free surface elevation, with respect to still water level was recorded continuously with wave height meters (WHM). Four resistance-type twin-wire WHM's were placed in the model at the following locations. The locations were chosen such that in principle the incoming bound, incoming free, the reflected free and reflected bound components may be separated. Besides the four wave gauges at a fixed position, two wave gauges were located on the measurement carriages.

During the operation quantities were measured by a number of instruments attached to two movable carriages. Moreover, four wave-gauges at a fixed position throughout the experimental programme measured the water elevation. The instruments on the carriage measured at a fixed horizontal and vertical position for about half an hour and were then moved to other locations. During each wave half-hour, exactly the same steering signal was used. The aim of this procedure was to use subsequent measurements to resolve the conditions at several locations at the profile and several distances from the bed, as if the measurements were made simultaneously. In order to assess this assumption of repeatability of the conditions, several point measurements were repeated. Variations can occur both as a result of changes in the conditions at the specific location along the profile due to the changing bottom profile and as a result of changes induced by variations in the positioning of the instruments with respect to

the ripples. From the comparisons made in these reports it appears that the variations in the time-mean parameters are small.

In Series A, the focus was on the collection of instantaneous velocity and concentration data at several locations along the beach profile and for varying distances from the sandy bed. The set-up of the measurement programme was so as to enable the identification of the spatial correlation (in both horizontal and vertical direction) of concentration, the time-dependent near-bottom response of the concentration to water velocity and the contribution of the various velocity components to the sediment fluxes. Series A consisted globally of two parts. The first part aimed at collecting data at various heights above the bed at eight selected horizontal positions ranging from the shoreline up to the toe of the profile. In the second part of series A, the focus was on horizontal correlation measurements. In those series the elevation of the instruments was 1cm above the ripple crests. The first carriage was located in the same vertical (same x-position) during all half-hour tests, whereas the second carriage was moved after every half-hour. Carriage 2 was first placed 15 cm onshore from carriage 1 and the final position was 70 cm from carriage 1. This procedure was performed at two locations at the profile.

Series B focused on the selective transport of placers of Zircon. Thin layers of Zircon were placed at several x-positions on the single-barred final profile of series A. In these experiments only the sediment profile and composition was measured.

The C-series aimed at measurements of selective transport processes. The series started again from a 1 in 40 beach, in which the upper 10 cm of the bed consisted of a mixture of 60% sand and 40% Zircon by mass. During runs hydrodynamic parameters and sediment concentrations were recorded; in between the runs, profile and sediment composition were measured.

The objective of the D-series was to test a new device to record “friction” sound. These experiments were carried out with still water on the end profile of Series C.

At specific time intervals (mostly the end of the day) profile measurements were conducted by an automatic sounding system. From these profiles, sediment transport rates could be inferred, such that the measurements can be used for sediment transport model and morphodynamic model verifications.

In the presented reports attention was paid to the calibration and validation of the measurements. A first analysis of the time-dependent results (Bosboom et al., 1999) aimed at identifying the relative importance of mean flow, long and short waves to the net sediment fluxes and transport. The recommended next steps are the actual in-depth analysis of the sediment response, the horizontal and vertical structure of velocity, concentration and sediment fluxes. Also parts of the time-averaged measurements are analysed (Koomans *et al.*, 1999) with attention to the distribution of the heavy mineral concentrations. Future research on the effects of density gradation will focus on the transport mechanisms and transport modes of the different minerals and will aim to describe the processes responsible for heavy mineral placer formation. The experiments to test a new instrument to determine median grain size from measured “friction” sound are analysed in depth and will be published.

## 6 References

- Bosboom, J. , Koomans, R.L. (2000) *Laboratory experiments on sediment dynamics and density gradation. Part II: Time-dependent measurements*. WLIDELFT HYDRAULICS report H2035.73.
- Bosboom, J., Koomans, R. & Reniers, A., (1999), *Laboratory experiments on suspended sediment concentration profiles*. In: Coastal sediments, Long Island, New York.
- Bosman, J. J., van der Velden, E. T. J. M. & Hulsbergen, C. H. (1987) *Sediment Concentration Measurement by Transverse Suction*. Coastal Engineering, **11**, pp. 353-370
- de Meijer, R. J. (1998) *Heavy minerals: from 'Edelstein' to Einstein*. Journal of Geochemical Exploration, **62**(1-3), pp. 81-103
- de Meijer, R. J., Stapel, C., Jones, D. G., Roberts, P. D., Rozendaal, A. & Macdonald, W. G. (1997) *Improved and New Uses of Natural Radioactivity in Mineral Exploration and Processing*. Exploration Mining Geology, **6**(No.1), pp. 105-117
- Klopman, G., (1995), *Active wave absorption, digital control systems for wave channels based on linear wave theory*. Report on desk study, Part II. Report H1684.33. WLIDelft Hydraulics.
- Klopman, G., (1998), personal communication.
- Koomans, R. L., Bosboom, J., de Meijer, R. J. & Venema, L. B., (1999), *Effects of density on cross-shore sediment transport*. In: Coastal sediments, Long Island, New York.
- Roelvink, J. A. & Stive, M. J. F. (1989) *Bar-generating cross-shore flow mechanisms on a beach*. Journal of Geophysical research, **94**(C4), pp. 4785-4800
- van Rijn, L. (1990) *Principles of sediment transport in rivers, estuaries and coastal seas* . Aqua publications, 335 pp.
- Venema, L. B., de Meijer, R. J., van Os, B. & Gieske, J. M. J., (1999), *In-situ characterisation of coastal and river sediment*. In: COPEDEC 99, **1** (Ed. by G. P. Mocke), pp. 324-334, Cape Town, South Africa.



# Appendices

## **Appendix A .**

# I Figures

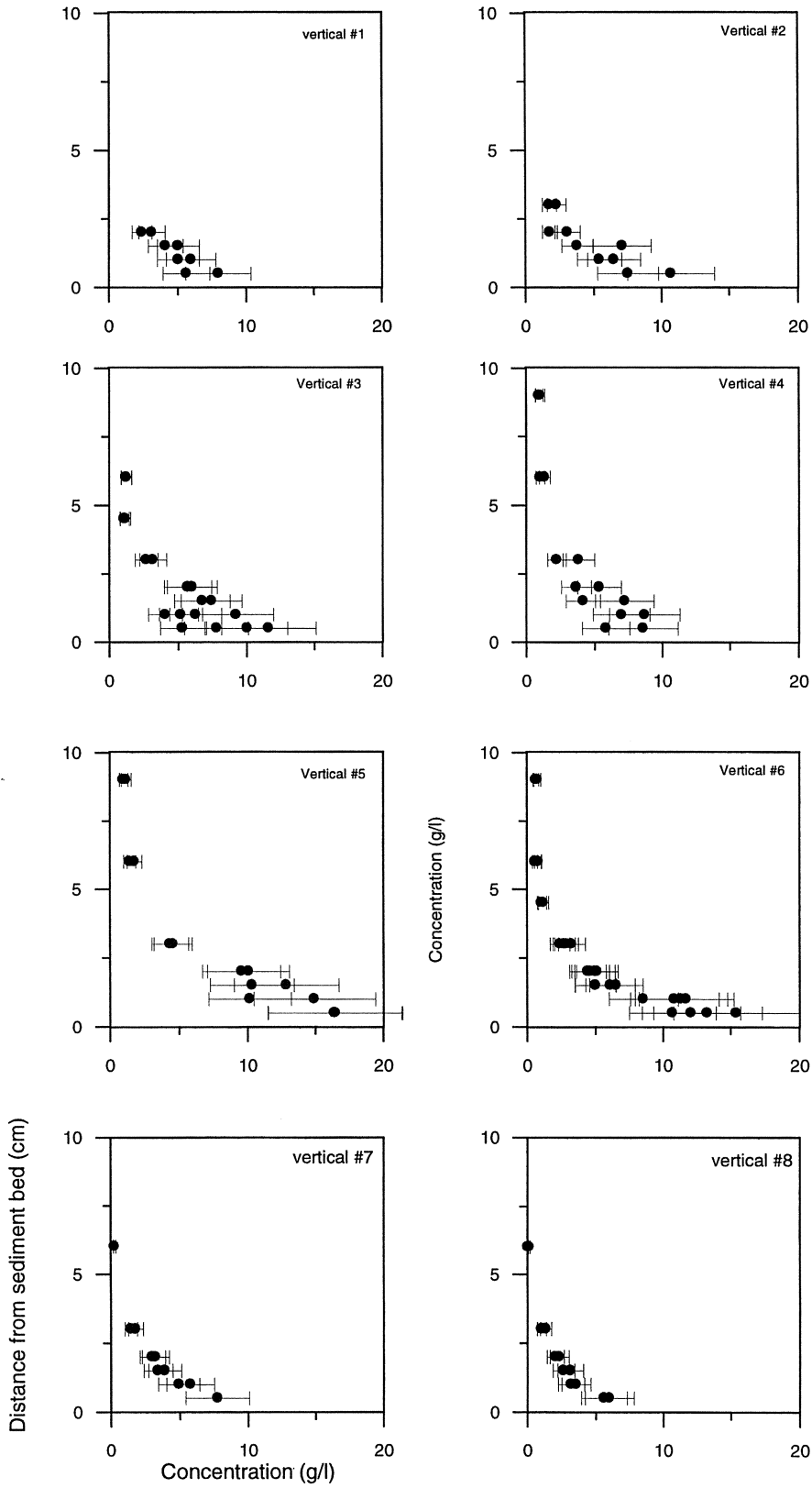


Figure 1.1: Suspended sediment concentration verticals for series A.

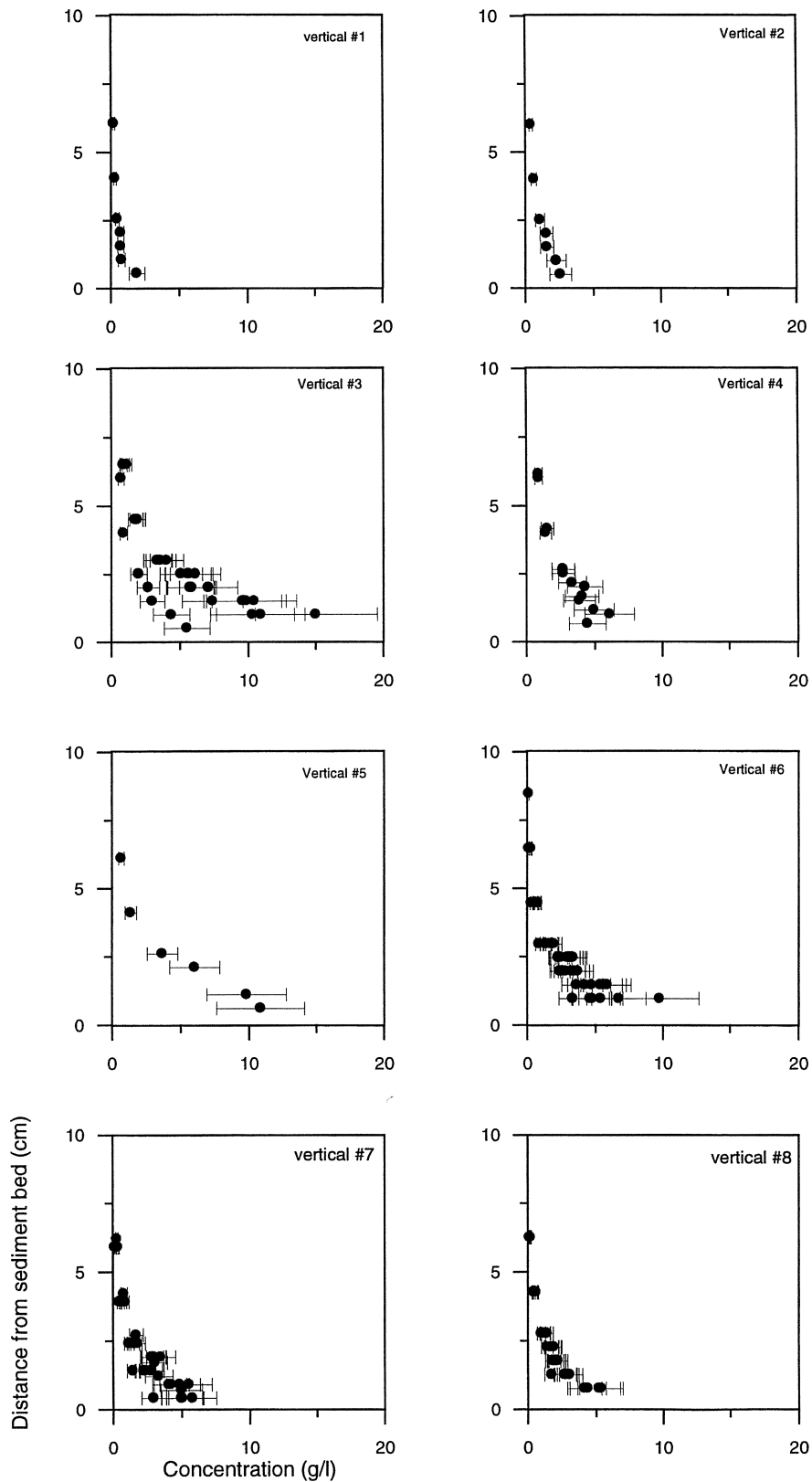


Figure 1.2: Suspended sediment concentration verticals for series C.

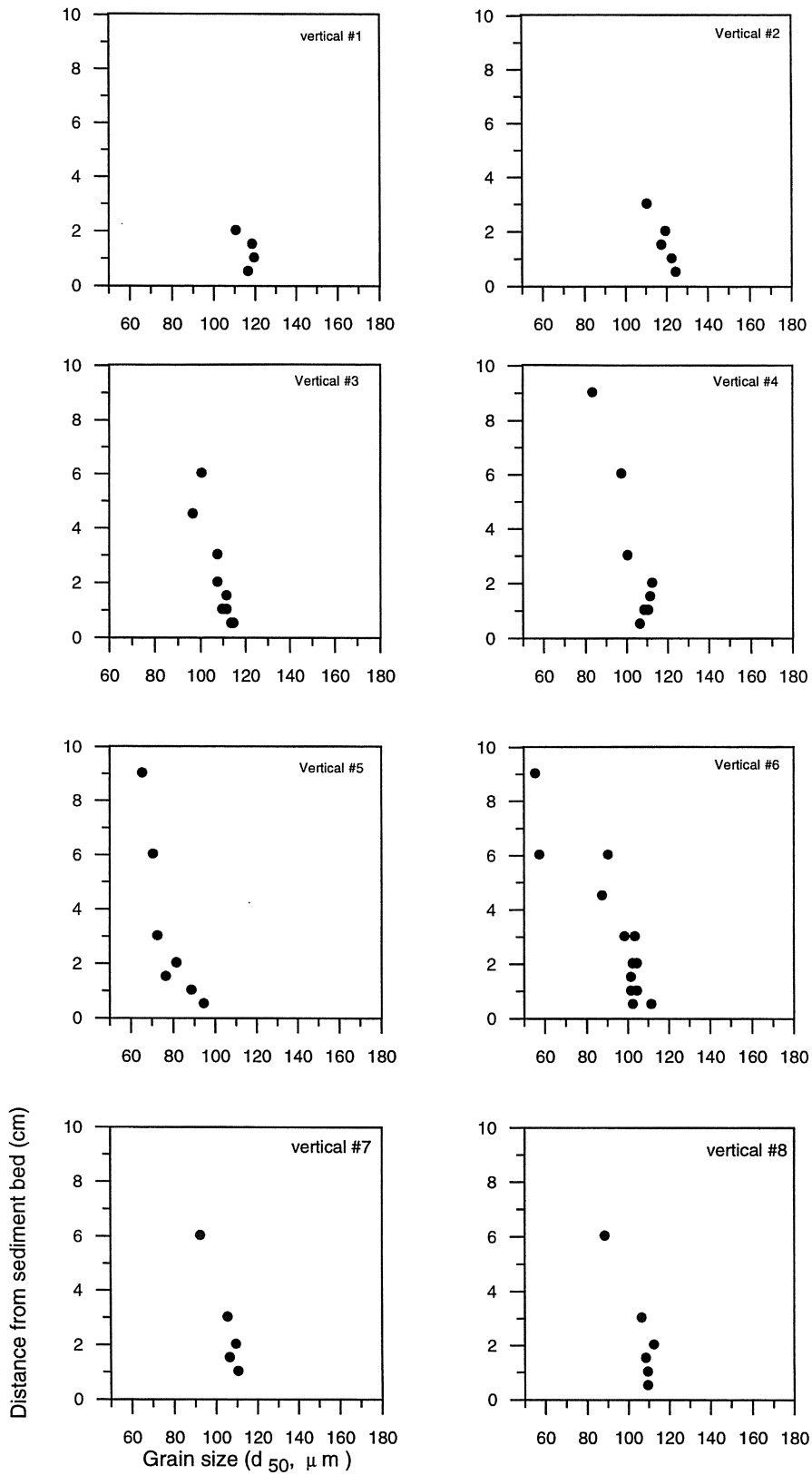


Figure 1.3: Elevation as function of grain size ( $d_{50}$ ) for the suspended sediments of series A.

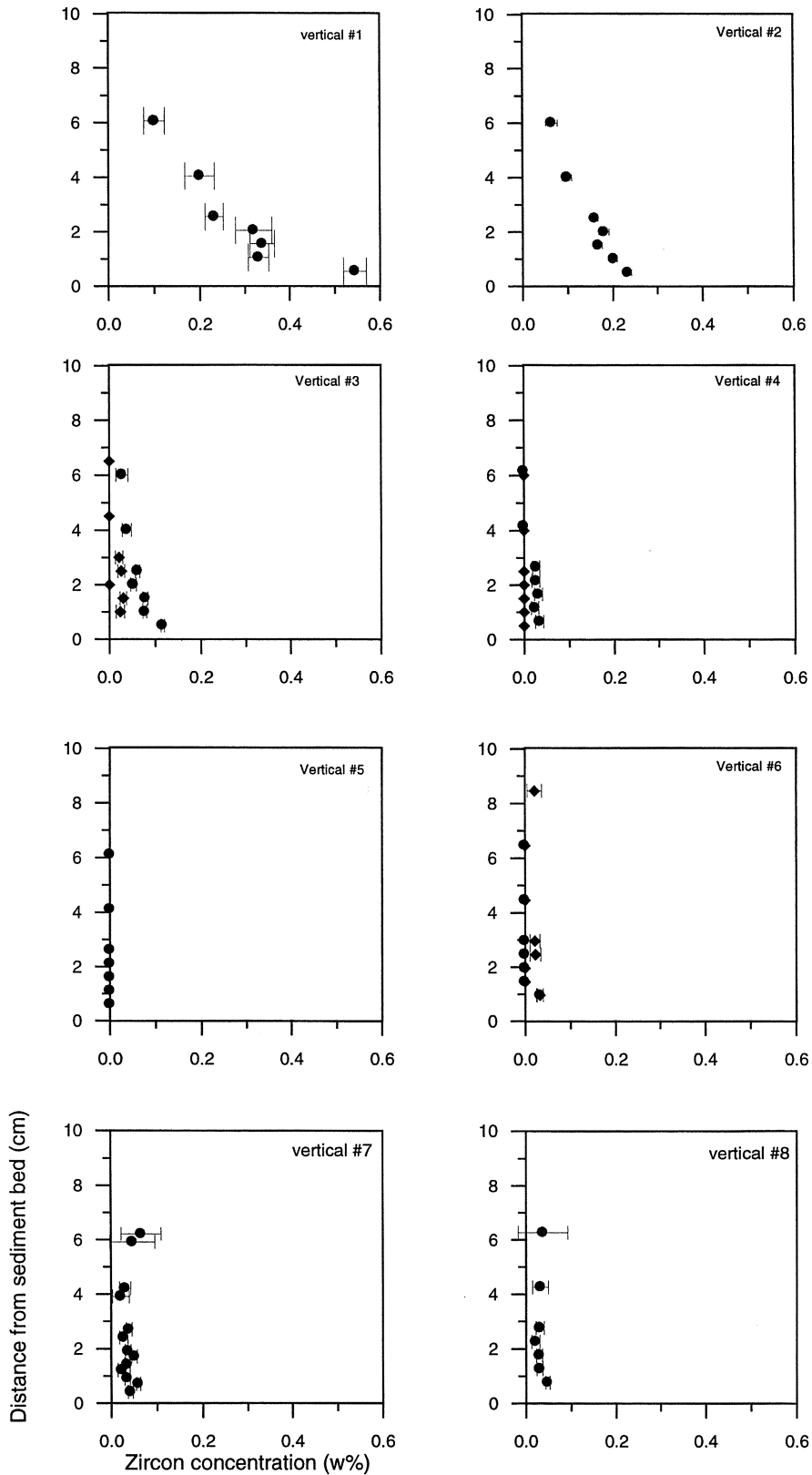


Figure 1.4: Elevation as function of Zircon concentration (weight percent) for the suspended sediments of series C.

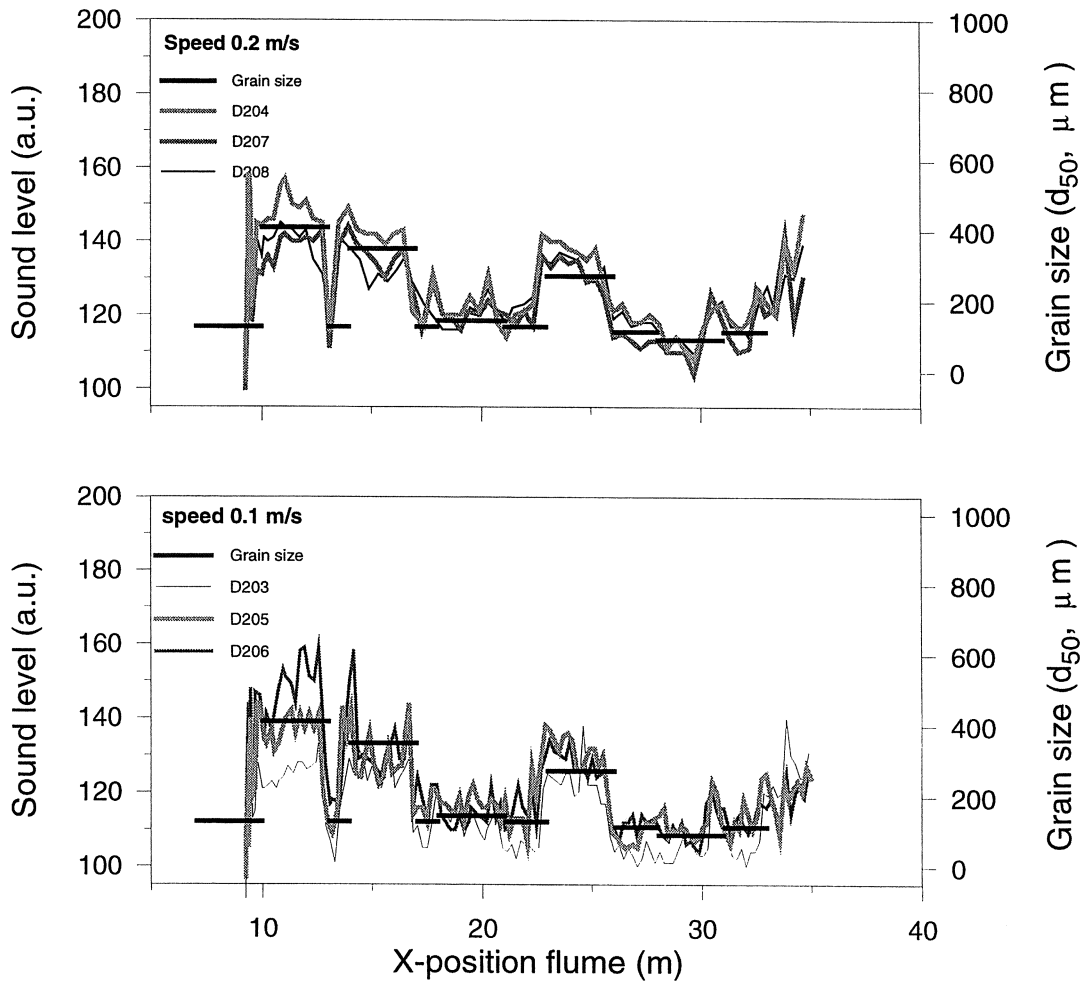


Figure 1.5: MEDUSA sound measurements and grain size variation of the patches along the profile of series D for two different towing speeds.

# Appendix B .



# I Overview of measurements

## A-series

Series A consisted globally of two parts. The first part aimed at collecting data at various heights above the bed at eight selected horizontal positions ranging from the shoreline up to the toe of the profile (Table 1.1).

Table 1.1: Positions of the measuring verticals

Vertical	x-position (m)
1	33
2	30.5
3	28
4	25.5
5	23
6	20.5
7	18
8	15.5

In first part of series A, half-hour measurements were made at the locations in Table 1.1 at different heights above the bed. In the second part of series A, the focus was on correlation measurements. In these experiments, the elevation of the instruments was 1 cm above the ripple crest. The first carriage was located at one position during all half-hour tests, whereas the second carriage was moved every half-hour (see Table 1.2). Carriage 2 was first placed 15 cm onshore from carriage 1 and the final position was 70 cm from carriage 1.

Table 1.2: Positions of carriage 2 in the correlation measurements and on-shore distance of carriage 2 with respect to carriage1.

Vertical	x-position (m)	$X_{car2} - X_{car1}$
4a	25.65	0.15
4b	25.75	0.25
4c	25.8	0.30
4d	25.85	0.35
4e	26	0.50
4f	26.1	0.60
4g	26.2	0.70
6a	20.65	0.15
6b	20.75	0.25
6c	20.8	0.30
6d	20.85	0.35
6e	20	0.50
6f	20.1	0.60
6g	20.2	0.70

Table 1.3: Positions of the carriages during each half-hour run of series A

Series name	carriage 1		carriage 2		remarks
	vertical	height (cm above bed)	height (cm above bed)	vertical	
%A100					<b>profile</b>
A101	8	0.5	0.5	7	<sup>12</sup>
A102	8	1	1	7	<sup>12</sup>
A103	8	1.5	1.5	7	<sup>12</sup>
A104	8	2	2	7	<sup>12</sup>
A105	8	3	3	7	<sup>1</sup>
A106	8	6	6	7	<sup>1</sup>
%a106					
A201	6	0.5	0.5	3	<sup>3</sup>
A202	6	1	1	3	
A203	6	1.5	1.5	3	
A204	6	2	2	3	
A205	6	3	3	3	
A206	6	6	6	3	
A207	6	4.5	4.5	3	
%a207					<b>profile</b>
A301	5	1.5	1.5	2	
A302	5	2	2	2	
A303	5	3	3	2	
A304	5	6	1	2	
A305	5	9	0.5	2	<sup>4</sup>
A306	5	0.5	0.5	1	
A307	5	1	1	1	
A308	3	0.5	1.5	1	
A309	3	1	2	1	
%a309					<b>profile</b>
A401	6	0.5	0.5 <sup>5</sup>	4	
A402	6	1	1	4	
A403	6	1.5	1.5	4	
A404	6	2	2	4	
A405	6	3	3	4	
A406	6	6	6	4	
A407	6	9	9	4	
%a407					<b>profile</b>
A501	5	1	1	5a	
A601	6	1	1 <sup>5</sup>	6a	<sup>6</sup>

<sup>1</sup> Due to velocity range of 10cm/s instead of 30 cm/s ADV1 and ADV2 signals contain spikes which can partly be removed by further post-processing

<sup>2</sup> Sampling volume ADV 6 mm instead of 9 mm

<sup>3</sup> signal OPC01 and OPC02 out of (analog output) range; percentages of time need to be assessed

<sup>4</sup> ADV01 a few moments close to water surface

<sup>5</sup> OpCon signal range larger than 10 V; further inspection on validity of peaks is necessary

<sup>6</sup> OPC01 signal not complete

Series name	carriage 1 vertical	height (cm above bed)	carriage 2 height (cm above bed)	vertical	remarks
A611	6	1	1 <sup>5</sup>	6a	
A602	6	1	1	6b	
A603	6	1	1 <sup>5</sup>	6c	
A604	6	1	1	6d	
A605	6	1	1 <sup>5</sup>	6e	
A606	6	1	1 <sup>5</sup>	6f	
A607	6	1	1 <sup>5</sup>	6g	
%a607					<b>profile</b>
A701	4	1	1	4a	<sup>7</sup>
A702	4	1	1	4b	
A703	4	1	1	4c	
A704	4	1	1	4d	
A705	4	1	1	4e	
A706	4	1	1	4f	
A707	4	1	1	4g	
%a707					
A801	8	1	1 <sup>5</sup>	7	
A802	8	3	3	7	
A803	8	6	6	7	
A901					<b>video</b>
A902					<b>video</b>
A903					<b>video</b>
A904					<b>video</b>
%a904					<b>profile</b>

Table 1.4: Measured vertical positions, name of the series and carriage number for vertical 1

Vertical	height (cm above bed)	series name	carriage
1	0.5	A306	2
1	1	A307	2
1	1.5	A308	2
1	2	A309	2

<sup>7</sup> Series A7\* 4 cm offshore from vertical 4

Table 1.5: Measured vertical positions, name of the series and carriage number for vertical 2

Vertical	height (cm above bed)	series name	carriage
2	0.5	A305	2
2	1	A304	2
2	1.5	A301	2
2	2	A302	2
2	3	A303	2

Table 1.6: Measured vertical positions, name of the series and carriage number for vertical 3

Vertical	height (cm above bed)	series name	carriage
3	0.5	A308	1
3	0.5	A201	2
3	1	A309	1
3	1	A202	2
3	1.5	A203	2
3	2	A204	2
3	3	A205	2
3	4.5	A207	2
3	6	A206	2

Table 1.7: Measured vertical positions, name of the series and carriage number for vertical 4

Vertical	height (cm above bed)	series name	carriage
4	0.5	A401	2
4	1	A402	2
4	1	A701 <sup>7</sup>	1
4	1	A702	1
4	1	A703	1
4	1	A704	1
4	1	A705	1
4	1	A706	1
4	1	A707	1
4	1.5	A403	2
4	2	A404	2
4	3	A405	2
4	6	A406	2
4	9	A407	2

Table 1.8: Measured vertical positions, name of the series and carriage number for the locations near vertical 4

Vertical height (cm above bed)	series name	carriage
4a 1	A701	2
4b 1	A702	2
4c 1	A703	2
4d 1	A704	2
4e 1	A705	2
4f 1	A706	2
4g 1	A707	2

Table 1.9: Measured vertical positions, name of the series and carriage number for vertical 5

Vertical height (cm above bed)	series name	carriage
5 0.5	A306	1
5 1	A307	1
5 1	A501	1
5 1.5	A301	1
5 2	A302	1
5 3	A303	1
5 6	A304	1
5 9	A305	1

Table 1.10 Measured vertical positions, name of the series and carriage number for the location near vertical 5

Vertical height (cm above bed)	series name	carriage
5a 1	A501	2

Table 1.11 Measured vertical positions, name of the series and carriage number for vertical 6

Vertical height (cm above bed)	series name	carriage
6 0.5	A201	1
6 0.5	A401	1
6 1	A202	1
6 1	A402	1
6 1	A601	1
6 1	A611	1
6 1	A602	1
6 1	A603	1
6 1	A604	1
6 1	A605	1
6 1	A606	1
6 1	A607	1
6 1.5	A203	1
6 1.5	A403	1
6 2	A204	1
6 2	A404	1
6 3	A205	1
6 3	A405	1
6 4.5	A207	1
6 6	A206	1
6 6	A406	1
6 9	A407	1

Table 1.12 Measured vertical positions, name of the series and carriage number for the locations near vertical 6

Vertical height (cm above bed)	series name	carriage
6a 1	A601	2
6a 1	A611	2
6b 1	A602	2
6c 1	A603	2
6d 1	A604	2
6e 1	A605	2
6f 1	A606	2
6g 1	A607	2

Table 1.13 Measured vertical positions, name of the series and carriage number for vertical 7

Vertical	height (cm above bed)	series name	carriage
7	0.5	A101	2
7	1	A102	2
7	1	A801	2
7	1.5	A103	2
7	2	A104	2
7	3	A105	2
7	3	A802	2
7	6	A106	2
7	6	A803	2

Table 1.14 Measured vertical positions, name of the series and carriage number for vertical 8

Vertical	height (cm above bed)	series name	carriage
8	0.5	A101	1
8	1	A102	1
8	1	A801	1
8	1.5	A103	1
8	2	A104	1
8	3	A105	1
8	3	A802	1
8	6	A106	1
8	6	A803	1

## C-series

Table 1.15: Names of the series and corresponding measuring verticals

Vertical	series name
-	c404 <sup>8</sup>
1	c401 <sup>9</sup>
2	c304
3	c201
3	c303
4	c302
4	c403
5	c301
6	c101 <sup>10</sup>
6	c204
7	c203 <sup>11,12</sup>
7	c402
8	c202

<sup>8</sup> Two hour wave duration; no measurements .

<sup>9</sup> ADV malfunctioning

<sup>10</sup> Half-hour measurement instead of hour measurement, ADV-file not complete

<sup>11</sup> 'Peilvoetje' in water during experiment

<sup>12</sup> no ADV data

## D-series

Table 1.16: Experimental conditions of the friction sound measurements of the D-series

Series	Water	Grain size	accelerometer	microphone	Speed (m/s)
D101	-	110 $\mu\text{m}$		+	0.1
D102	-	110 $\mu\text{m}$		+	0.2
D103	-	110 $\mu\text{m}$	+		0.1
D104	-	110 $\mu\text{m}$	+		0.2
D201	-	Mix	+		0.1
D202	-	Mix	+		0.1
D203	+	Mix	+		0.1
D204	+	Mix	+		0.2
D205	+	Mix		+	0.1
D206	+	Mix		+	0.1
D207	+	Mix		+	0.2
D208	+	Mix		+	0.2

Table 1.17: Distribution of grain size patches of the D-series

Begin x (m)	End x (m)	D <sub>50</sub> ( $\mu\text{m}$ )	D <sub>10</sub> ( $\mu\text{m}$ )	D <sub>90</sub> ( $\mu\text{m}$ )
37.1	36.2	Gravel	Gravel	Gravel
36	33	197	145	267
31	28	92	57	144
26	23	273	198	404
21	18	146	93	243
17	14	350	191	597
13	10	411	314	559



## Profile evolution

Tables showing profile evolution for the different profile measurements.

Table 1.18: Cumulative times of profile evolution for the A-series

Profile	time of profile evolution (s)	time of profile evolution (h)
A106	14468	4:01:08 ↵
A207	29228	8:07:08
A309	48047	13:20:47
A407	62684	17:24:44 ↵
A607	81503	22:38:23
A707	96140	26:42:20
A904	106613	29:36:53 ↵

Table 1.19: Cumulative times of profile evolution for the B-series

Profile	time of profile evolution (s)	time of profile evolution (h)
B101	1820	0:30:20
B102	5461	1:31:01
B104	12743	3:32:23

Table 1.20: Cumulative times of profile evolution for the C-series

Profile	time of profile evolution (s)	time of profile evolution (h)
C101	2071	0:34:31
C201	5962	1:39:22
C302	25417	7:03:37
C402	40981	11:23:01
C404	52404	14:33:24

# Appendix C .

# I Measurements of sediment composition

## I.1 Introduction

### I.1.1 Interaction of $\gamma$ -radiation and matter

When  $\gamma$ -rays penetrate matter, they can interact with atoms of the medium in various ways. The two main interaction processes in the relevant energy range of the  $\gamma$ -ray studies of natural radioactivity,  $10\text{keV} < E_\gamma < 3\text{MeV}$ , are 1) photo-electric absorption and 2) Compton scattering. The third interaction process, pair-production, does not play a significant role at these energies. In all processes, free electrons are generated by the photons. These free electrons excite the lattice electrons of the material. In a photon detection crystal, the excited electrons produce a light flash that can be measured with a photo-multiplier tube (PMT). Next chapter will describe what the effect of the two relevant interaction processes is on the measured  $\gamma$ -ray spectrum for mono-energetic photons and a photon continuum (Debertin and Helmer, 1998).

#### Photo-electric absorption

In the photo-electric absorption process, all of the photon energy is absorbed and transferred to a so called photo-electron. This electron is ejected from the atom with an energy  $E_e$  equal to:

$$E_e = E_\gamma - E_b, \quad (1.1)$$

where  $E_\gamma$  is the energy of the incident  $\gamma$ -ray and  $E_b$  the binding energy of the electron in its original shell. When the photo-electric absorption effect of a mono-energetic photon bundle is measured, the absorbed  $E_\gamma$ -spectrum will result in a sharp peak, the so-called photo peak. The amplitude of the peak is a function of the intensity of the  $\gamma$ -ray bundle and the absorption properties of the material. The energy position of the peak is a function of the energy of the photons.

#### Compton scattering

In the Compton scattering process, only a portion of the photon energy is transferred to an electron and the remainder is carried away by a secondary photon ( $E_\gamma'$ ). The energies of the outgoing electron and secondary photon are related to the scattering angle (Figure 1.1). After scattering, the secondary photon can be absorbed by photo-electric absorption or scattered again by the Compton scattering process. It is possible that it scatters out of the medium without depositing its full energy. In an energy spectrum of a mono-energetic  $\gamma$ -ray bundle, the scattering process will lead to a distribution of energies lower than the energy of the incident  $\gamma$ -ray: the Compton continuum (Figure 1.2). The Compton continuum of Figure 1.2 is composed of photons that are Compton scattered in the detector (releasing their full energy in

different events or only releasing part of their energy and scattering out of the detector) and of photons that were Compton scattered in the surrounding medium, and entered the detector as scattered photons with a lower energy than the original photon.

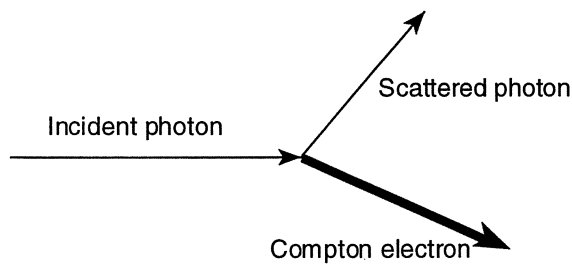


Figure 1.1: Schematisation of the Compton scattering process.

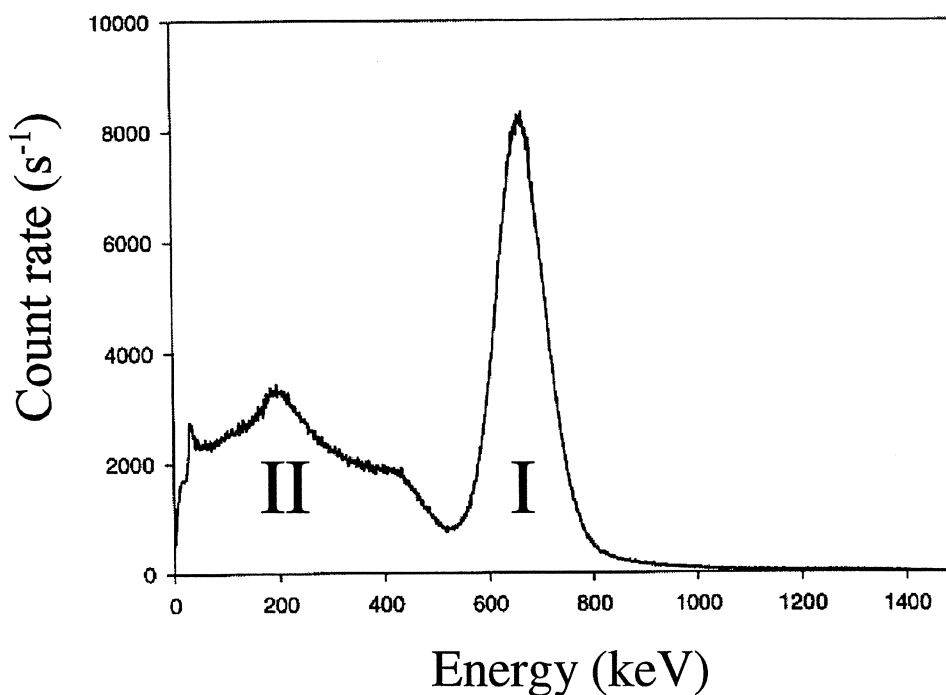


Figure 1.2: The contributions of different interactions to a  $\gamma$ -ray spectrum of a monoenergetic source. All events that deposit their full energy in the detector, i.e. events that undergo photo-electric absorption will show as a peak in the  $E_\gamma$ -spectrum: the photopeak (I). Events that interact via Compton scattering, show up in the Compton continuum (II).

### 1.1.2 Attenuation of $\gamma$ -rays

If a beam of mono-energetic photons (in a 1-D case) passes through an absorber with thickness  $z$ , photons undergo energy loss from the layer in the beam direction due to the above described processes. The probability per unit path length that a  $\gamma$ -quant is removed from the beam depends on the energy of the  $\gamma$ -quant and the density and atomic number of the medium and is described by  $\mu$ : the linear attenuation coefficient. The attenuation coefficient will decrease with increasing photon energy, which means that high energy photons have a larger possibility to pass an absorber undisturbed than low energy photons. Since both the

photo-electric effect and Compton scattering remove photons from the beam, the total linear attenuation coefficient is the sum of the two partial attenuation coefficients:

$$\mu = \tau_{photo-electric} + \sigma_{Compton} \quad (1.2)$$

The number of photons ( $N$ ) that are transmitted through the absorber are given by:

$$N = N_0 e^{-\mu z} \quad (1.3)$$

The linear attenuation coefficient has the dimension  $\text{cm}^{-1}$  and varies with the density  $\rho$  of the absorber. A more general expression with the mass attenuation coefficient  $\mu'$  (defined  $\mu' = \mu \rho^{-1}$ ), with the dimension  $\text{g}^{-1} \text{cm}^2$  reads:

$$N = N_0 e^{-\mu' \rho z} \quad (1.4)$$

The mass attenuation coefficient for a mixture of elements can be obtained by:

$$\mu'_{mixture} = \sum_i w_i \mu'_i \quad (1.5)$$

Where  $w_i$  is the weight fraction of element  $i$  (with mass attenuation coefficient  $\mu'_i$ ) in the mixture.

### 1.1.3 The $\gamma$ -ray spectrum

Previous chapters described the shape of an  $E_\gamma$ -spectrum, resulting from a mono-energetic source. In nature however,  $\gamma$ -photons with different energies are emitted and the  $\gamma$ -energy spectrum will be more complex than described in Figure 1.2. When photons from a source with different energies hit a  $\gamma$ -ray detector crystal, the resulting spectrum will be composed of a number photo-peaks and different Compton continua. The photo-peak and the Compton continuum of the lower energy lines are superimposed on the Compton continuum of the higher energetic  $\gamma$ -ray. Moreover, photons resulting from cosmic background radiation will contribute to the Compton continuum.

#### Build up

In the case of a point source in front of a detector, the Compton energies in the spectrum originate from the Compton-scattered  $\gamma$ -rays in the detector itself. However, when a sediment layer is placed before the detector (Figure 1.3), also  $\gamma$ -rays that are Compton-scattered within the sediment (depending on the Compton attenuation coefficient) will reach the detector where they can react via Compton scattering or the photo-electric effect. This means that  $\gamma$ -rays found in the photo-peak did not have any interactions in the sediment and had photo-electric absorption within the detector. Also photons that enter the detector via back-scattering in water, will end in the Compton continuum. The  $\gamma$ -rays found in the Compton continuum have been Compton scattered either in the sediment, water and or the detector. The

measured photons that are Compton scattered in the sediment and water column, are called build-up. The amount of build-up is a function of the geometry of the detector, the thickness of the sediment  $z$  and the attenuation coefficient  $\mu$  and density  $\rho$  of the sediment.

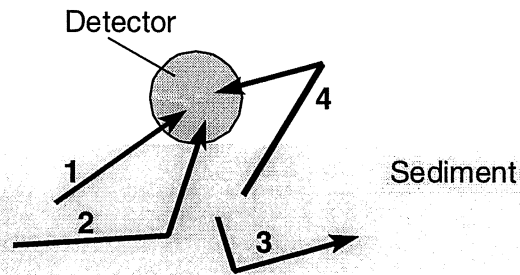


Figure 1.3: Schematic presentation of the various contributions to the  $E_\gamma$ -spectrum, from a sediment source under water. 1) Direct contribution, 2) Compton scattered photon, from the sediment, 3) no contribution, 4) Compton scattered in the water column.

## 1.2 Rendement

Not all photons that are emitted from the sediment are detected by the detector. The rendement of the detector system depends on the geometry of the detector and the detector efficiency.

### 1.2.1 Solid angle and geometry

When a scintillation crystal is placed on a sediment bed, only half of the detector “faces” the radiation coming from the sediment and the “effective surface” of the detector will be more or less half the actual detector surface. For a specific volume of sediment in the bed beneath the detector, photons will be isotropically transmitted (360 degrees) but only part of these photons will end up in the detector (Figure 1.4). The probability that emitted photons will end up in the detector, depends mainly on the distance between detector and sampling volume (Figure 1.4) and is parameterised by the solid angle ( $\Omega$ ).

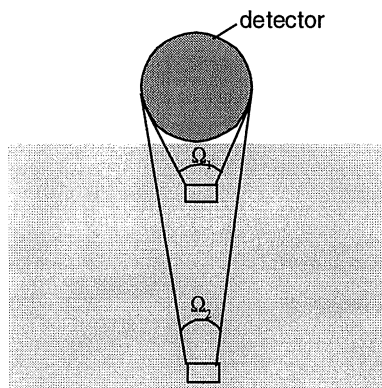


Figure 1.4: A detector placed on sediment. The solid angle ( $\Omega$ ) decreases with increasing distance from the detector.

The measurements in the flume and calibration measurements were done on a sediment bed that was not infinitely extending to the sides. Since the view of the detector will extend through the area without sediment, this will influence the relation between sediment height and measured count rate.

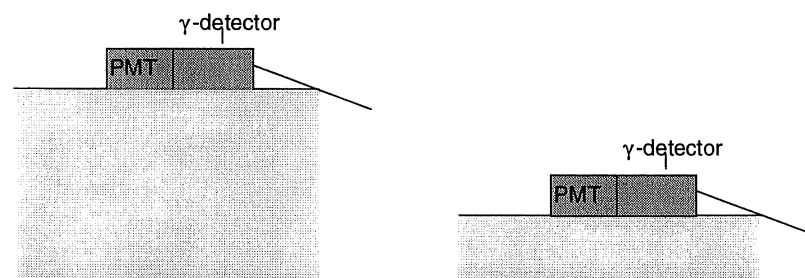


Figure 1.5: Schematic presentation of the cross-width detector set-up in the flume and "view" of the detector.

In the experiments in the Scheldt flume, the detector was placed on a sledge on top of the sediment bed (Figure 2.1). To this sledge a piece of lead was attached to keep the sledge in contact with the sediment. This 5mm thick piece of lead was placed between the sediment and detector and has shielded part of the radiation. This shielding is energy dependent and will decrease accordingly the amount of  $\gamma$ -rays detected. The PVC material of the sledge was very thin which gives no effect on the measured  $\gamma$ -ray intensity.

### 1.2.2 Detector efficiency

The  $\gamma$ -rays emitted by the radionuclides of the sediment may undergo several interactions before they reach the scintillation crystal (see paragraph 1.1.1). The  $\gamma$ -rays are emitted isotropically and the detector only covers a part of the  $4\pi$  solid angle. Moreover not all  $\gamma$ -rays hitting the detector will interact. For these reasons, detector efficiencies are in general <100%.

### 1.2.3 Gamma-ray spectra

Sediments contain the  $\gamma$ -ray emitting radionuclides of  $^{40}\text{K}$  and decay products of  $^{232}\text{Th}$  and  $^{238}\text{U}$ . One  $\gamma$ -ray is emitted by  $^{40}\text{K}$ , whilst in the decay series of Th and U several  $\gamma$ -rays with different intensities are emitted. A  $\gamma$ -ray spectrum of Zircon that contains these radionuclides is presented in Figure 1.6.

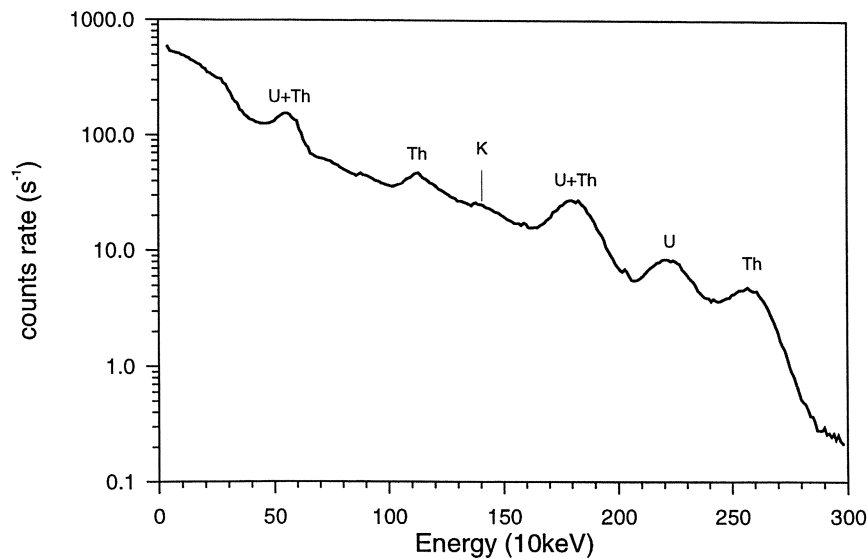


Figure 1.6: A  $\gamma$ -ray spectrum of Zircon measured with the MEDUSA system. At each peak is indicated which decay series contributes most to the peak.

The intensities are constant for lines within one decay series. Different concentrations of K, Th and U lead therefore not to a different set of lines but only to partially different intensities. In the case of measurements of the activity concentrations of the sediment, the source of the  $\gamma$ -rays will also act as a sink of  $\gamma$ -rays. Not all photons emitted from the sediment will reach the detector with their original energy and direction, since the photo-electric effect and Compton interactions in the sediment can occur. The part of the photons that are absorbed in the sediment itself are absorbed by “self-attenuation”. This self-attenuation process is a function of the path length of the photons in the sediment (the thickness of the sediment) and the attenuation coefficient  $\mu$ . Not only build up from the sediment contributes to the measured spectrum; also build up from Compton-scattered photons in the water will contribute (Figure 1.3). This implies that the photo-peak to Compton ratios for each line will be effected to the effective thickness of the sediment and the atomic number  $Z$  of the components. This means that in principle, the precise shape of the gamma-ray spectra will depend on the Zircon concentration in the mixture. In practice, fortunately, these effects are of higher-order and other effects are of larger importance.

Thus far, we considered homogeneously mixed sediment. In nature, however, sediments are only rarely mixed homogeneously mixed and stratification of sediments will occur. This stratification will influence the attenuation coefficient and when the sediment have different radiometric properties, also the source term will change throughout the sediment.

In principle, the behaviour of  $\gamma$ -radiation in the sediment bed is a complex system and its precise description is far from trivial. At the moment, simple models that describe this relation accurately are not present and Monte Carlo simulations are needed for a better understanding and description of the  $\gamma$ -ray spectra. In the following we will describe a model parameterisation in which the effective mass attenuation coefficient,  $\mu$ , and the sediment thickness are the important parameters.



### 1.3 Model parameterisation

Thus far in radiometric measurements with MEDUSA, an efficiency calibration is used to determine the relation between the measured  $\gamma$ -ray intensity and the activity concentration of radionuclides in the sample under the assumption of a homogeneous layer of sediment. This efficiency calibration is measured for several geometries and thereby contains already corrections for self-absorption in the sample and the effects of the geometry.

In present data analysis, we focus on an accurate derivation of the activity concentrations of the sediment bed from the measured activity concentrations and not on a better understanding of the physical mechanisms. Since an accurate 3-D model for these type of measurements is presently not available, the parameterisation will be based on 1-D model. Calibration measurements will be used to validate this parameterisation and to determine effective parameters.

In this section we first derive a description for a homogeneous layer and subsequently extend the description to a two homogenous-layer configuration. In this description, we assume that the effect of varying sediment thickness on the measured activity concentrations can be described by a 1-D model (Debertin and Helmer, 1989) and that effects of a natural 3-D configuration (build-up, variation in geometry) can be described in effective parameters. Instead of presenting activity concentrations for  $\gamma$ -lines of different energies, total count rate is used. The total count rate is the total number of counts per second of a defined part of a  $E_\gamma$  spectrum (ROI). By expressing activity concentrations in total count rate, information is integrated over the various photo-peaks and includes also the Compton continuum. With this description, the energy dependence of the mass attenuation coefficient is incorporated in an effective value. In the calibration procedure, the validity and effects of these approximations will be considered in more detail

#### 1.3.1 One layer

We assume that a detector is placed on a homogeneous plane source (a bed of sediment) with thickness  $z$  (cm). In a 1-D approximation of the radiation field, all  $\gamma$ -rays are assumed to be normal to the source surface. The number of counts ( $N$ ) measured in the detector can be described by an equation similar to equation ( 1.4 ):

$$N = \int_0^z \frac{I_{source}}{z} \epsilon e^{-\mu' \rho z} dz, \quad (1.6)$$

where  $I_{source}$  ( $s^{-1}$ ) is the intensity of the sediment (which is an extensive quantity, scaling linear with the sediment thickness),  $\epsilon$  is the efficiency of the detector in this particular geometry,  $\mu'$  the mass attenuation coefficient of the material ( $cm^2 g^{-1}$ ) and  $\rho$  the density ( $gcm^{-3}$ ). The value of  $I_{source}$  is the sum of all the emitted gamma-rays of  $^{40}K$ ,  $^{232}Th$  and  $^{238}U$  and will be a function of the activity concentrations of the three radionuclides.

For a very thin layer of sediment with thickness  $z$  the intensity  $I_{source}$  can be described by:

$$I_{source} = \int_0^z dI_{source} = \int_0^z dL_{source} dz, \quad (1.7)$$

with:

$$L_{source} = \frac{I_{source}}{z} \quad (1.8)$$

and  $L_{source}$  is the specific intensity per unit thickness sediment.

If we substitute equation (1.8) in equation (1.6) and integrate equation (1.6), the measured count rate on top of a layer of sediment with thickness  $z$  can be described by:

$$N(z) = \int_0^z L \mathcal{E} e^{-\mu' \rho z} dz = \frac{L \mathcal{E}}{\mu' \rho} (1 - e^{-\mu' \rho z}). \quad (1.9)$$

In sediment transport, most changes occur in the upper “active” layer. In this layer sediment are sorted and concentrated, while in the lower lying sediments the composition remains equal. To describe this system, an extra step is needed.

### 1.3.2 Two layers

Assume two layers of sediment  $z_1$  and  $z_2$  (Figure 1.7) which emit per second and unit volume  $L_1$  and  $L_2$  gamma rays. These sediments have densities  $\rho_1$  and  $\rho_2$  (in  $\text{gcm}^{-3}$ ) and mass attenuation coefficients  $\mu'_1$  and  $\mu'_2$  (in  $\text{cm}^2 \text{g}^{-1}$ ), respectively.

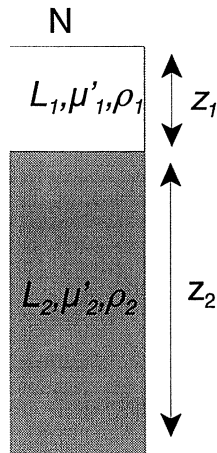


Figure 1.7: schematisation of two layers, with thickness  $z_1$  and  $z_2$ , mass attenuation coefficients  $\mu_1$  and  $\mu_2$ , densities  $\rho_1$  and  $\rho_2$  and specific activities  $L_1$  and  $L_2$ .

The measured count rate on top of the sediment for 2 superimposed layers with thickness  $z_1$  and  $z_2$  (see figure 1), can be described by a parameterisation similar to that of equation (1.9). However, an extra term comes in due to the attenuation of photons from layer  $z_2$  by layer  $z_1$  and the measured count rate from layer with thickness  $z_1$ :

$$N(z_2, z_1) = \left( L_2 \mathcal{E} \frac{(1 - e^{-\mu'_2 \rho_2 z_2})}{\mu'_2 \rho_2} \right) e^{-\mu'_1 \rho_1 z_1} + L_1 \mathcal{E} \frac{(1 - e^{-\mu'_1 \rho_1 z_1})}{\mu'_1 \rho_1}. \quad (1.10)$$

In the present experiments, it is assumed that the total sediment bed at time  $t=t_0$  is homogeneously mixed and represents the properties of layer 2. Therefore the count rate measured from the underlying sediment (with specific count rate  $L_2$ ) is known to be  $N_2$  and equation (1.9) can be rewritten to:

$$N(z_2, z_1) = N_2 e^{-\mu'_1 \rho_1 z_1} + L_1 \varepsilon \frac{(1 - e^{-\mu'_1 \rho_1 z_1})}{\mu'_1 \rho_1}. \quad (1.11)$$

In present experiments, the quantity of interest is the Zircon concentration per unit volume. This quantity is defined as the ratio of the measured total counts rate, relative to the total counts rate  $N_{zirc}^\infty$  of an infinite thick pure Zircon bed in an equal geometry:  $m_{zirc} = \frac{N(z_2, z_1)}{N_{zirc}^\infty}$

and

$$m_{zirc} = \frac{N_2 e^{-\mu'_1 \rho_1 z_1} + L_1 \varepsilon \frac{(1 - e^{-\mu'_1 \rho_1 z_1})}{\mu'_1 \rho_1}}{N_{zirc}^\infty}. \quad (1.12)$$

Since the calibration measurements for zircon were done for an infinite bed, the measured count rate for Zircon can be expressed as:

$$N_{zirc}^\infty = \frac{L_{zirc} \varepsilon}{\mu'_{zirc} \rho_{zirc}}. \quad (1.13)$$

Substituting equation ( 1.13 ) in ( 1.12 ) gives:

$$m_{zirc} = \frac{N_2 e^{-\mu'_1 \rho_1 z_1}}{N_{zirc}^\infty} + \frac{L_1}{L_{zirc}} \frac{\mu'_{zirc} \rho_{zirc}}{\mu'_1 \rho_1} (1 - e^{-\mu'_1 \rho_1 z_1}). \quad (1.14)$$

The quantities  $m_{zirc}$  and  $\frac{N_2}{N_{zirc}^\infty}$ , the Zircon concentration of the initial bed, are known.

Therefore the quantities  $\frac{L_1}{L_{zirc}}$  and  $\mu'_1 \rho_1$  have to be derived. These quantities depend both on the amount of Zircon in layer 1 and their values are derived iteratively.

## Variation in thickness of layer $Z_2$

In the experiments, only the upper 10cm of the sediment consisted of the Quartz-Zircon mixture. Below this mixture, pure Quartz was present which is assumed to give no significant contribution to the count rate. At time  $t=t_1$ , the total thickness of the mixed sediment bed, is composed of the layers  $z_1$  and  $z_2$  (see Figure 1.8). For the data analysis of these experiments, the thickness of  $z_1$  is chosen as a constant (5 cm). The thickness of  $z_2$  is not constant but depends on the chosen thickness of the layer of interest,  $z_1$  and the variation in bed level. For the case of accretion, the thickness of layer  $z_2$  will be larger at  $t_1$  than at  $t_0$  and the count rate coming from this layer will be higher. In the erosion case, the thickness of layer  $z_2$  at  $t=t_1$  will be smaller than the thickness at  $t=t_0$  and hence the count rate from this thickness of sediment will be lower (Figure 1.8).

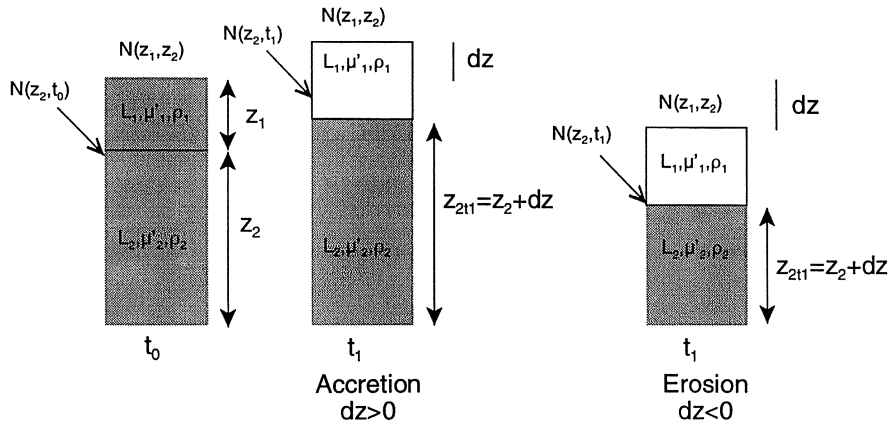


Figure 1.8: Schematisation of the morphologic variation and corresponding total count rate  $N_2$  for accretional and erosional cases. In this schematisation,  $z_1$  is constant.

The total number of counts measured from the sediment mixture at  $t_0$ , can be written as:

$$N(z_2, t_0) = L_2 \mathcal{E} \frac{(1 - e^{-\mu'_2 \rho_2 z_2})}{\mu'_2 \rho_2}. \quad (1.15)$$

At  $t=t_1$ , the thickness of layer  $z_2$  will be changed (Figure 1.8), while the specific activity of the sediment ( $L_2$ ) did not change. The total number of measured counts can be written as:

$$N(z_2, t_1) = L_2 \mathcal{E} \frac{(1 - e^{-\mu'_2 \rho_2 (z_2 + dz)})}{\mu'_2 \rho_2}. \quad (1.16)$$

Substituting equation (1.9) into (1.16) gives the relation between the measured count rate at  $t_0$ , the thickness of  $z_2$  and the desired parameter: the total count rate that would have been measured on top of the sediment layer with thickness  $z_2$  at  $t=t_1$ :

$$N(z_2, t_1) = N_{2t_0} \frac{(1 - e^{-\mu'_2 \rho_2 (z_2 + dz)})}{(1 - e^{-\mu'_2 \rho_2 z_2})}. \quad (1.17)$$

By substituting equation (1.17) into equation (1.14), the Zircon concentration per thickness of sediment can be calculated.

### Maximum depth of penetration

An interesting parameter is the maximum depth of visibility of the MEDUSA system in the sediment. This depth is the maximum depth up to where a significant percentage of  $\gamma$ -rays reaches the detector without interaction. To determine the percentage of  $\gamma$ -rays that reaches the detector without interaction

$$p \approx \frac{L - N(z)}{L}, \quad (1.18)$$

the sediment properties must be accounted for.

For an “infinite” sediment thickness, the relation between measured a count rate and the specific activity of the sediment, can be expressed as:

$$\lim_{z \rightarrow \infty} N(z) = L\varepsilon e^{-\mu' \rho z} \quad (1.19)$$

and substituting equation (1.19) in (1.18), the maximum depth of penetration ( $z_{\infty}$ ) can be determined once the needed precision (the percentage of  $\gamma$ -rays that still is detected) is defined:

$$\frac{-\ln p}{\mu' \rho} = z_{\infty}. \quad (1.20)$$

## 2 Calibration

To determine the accuracy of the formalism and to establish the “effective” parameters, derived in chapter 1.3, the system is calibrated in the flume.

### 2.1.1 Overview of calibration measurements

To calculate the effective attenuation coefficients for Quartz and Zircon, MEDUSA was calibrated for the geometry of the experiment. Boxes with varying thickness of Quartz and Zircon were placed at the end of the flume (at location  $x=7\text{m}$ ) at a water depth of 70 cm. The buckets had a size of  $0.7 \times 0.3\text{m}$ . The detector was placed on the sledge in the same geometry as during the experiment. On the PVC sledge, a small piece of wood with 2mm of lead was attached to prevent the sledge from floating. This lead was placed between the sediment and detector as similar to the actual measurements as possible. Since on both sides of the flume, different walls were located (one of concrete with a possible background concentration and one wall of PVC, the D (“drukleiding”) and W (“wand”)-side respectively), the measurements were repeated on both sides of the flume. These calibration measurements comprised recordings of 15 minutes, yielding sufficient statistics.

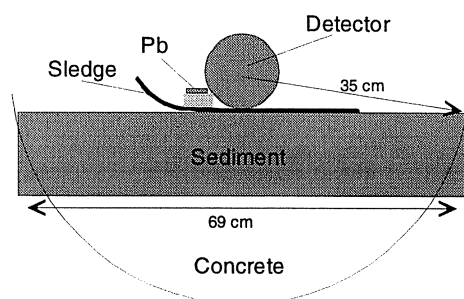


Figure 2.1: Set up of the calibration measurements. The detector is placed on the sledge on the sediment. A piece of wood with on top 2mm of lead is placed on one side of the sledge similar to the set up in the experiments. The circle denotes the “view” of the detector for  $\gamma$ -rays with a penetration depth of 35cm.

Table 2.1: Calibration measurements of homogenous bed of varying thickness but with constant sediment composition. The D/W notation in the filenames point to the measurements at both sides (d and w side) of the flume.

Filename	Thickness Zircon (cm)	Thickness Quartz (cm)
CaliD/W201	0	
CaliD/W202	3	
CaliD/W203	6.5-7	
CaliD/W204	10.8	
CaliD/W205	16.8	
CaliD/W206	22.8	
CaliD/W301		3
CaliD/W302		7
CaliD/W303		12
CaliD/W304		17.8
CaliD/W305		24
CaliD/W401	12	2
CaliD/W402	12	7
CaliD/W403	12	12
CaliD404	12	1

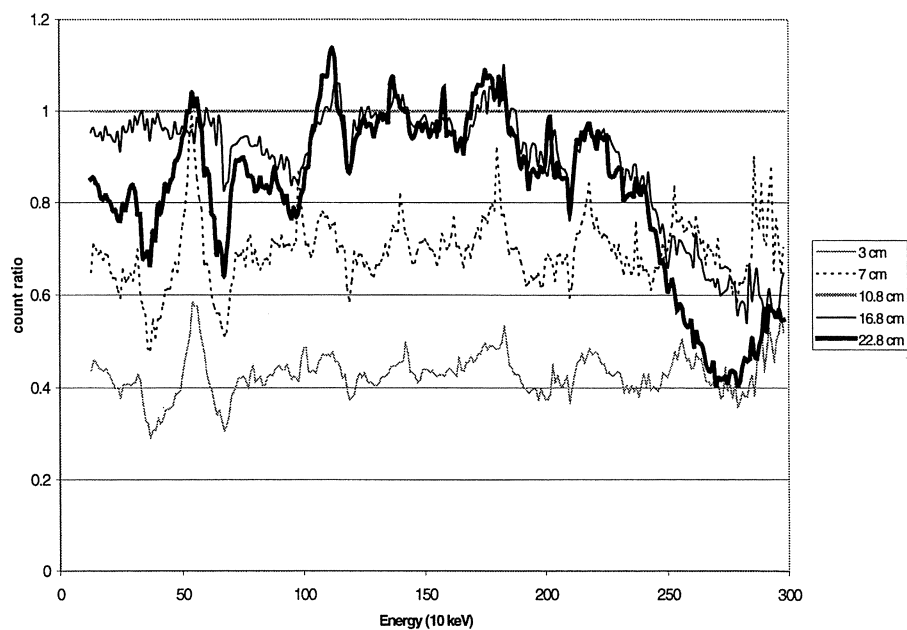


Figure 2.2:  $E_\gamma$  spectra of varying thickness of Zircon normalised on the  $E_\gamma$ -spectrum of 10.8 cm of Zircon.

### 2.1.2 Attenuation coefficients for Quartz and Zircon

The  $E_\gamma$ -spectra of the calibration measurements of Zircon are presented in Figure 2.2. These results present the ratios of the spectra with the spectrum of the Zircon bed with a thickness of 10.8 cm. The general trend in the spectra of 3cm and 7cm of Zircon shows a gradual increase in count rate with increasing sediment thickness. This implies that the shape of these

spectra is almost similar to that of the sediment bed with a thickness of 10.8 cm. The fluctuations in the signals of 3 and 7 cm are probably the result of small mismatches in the energy stabilisation between these spectra and the spectrum of 10.8 cm. However, these fluctuations are not assumed to be of importance. The measurements on the Zircon beds of 16.8 and 22.8cm show a different behaviour with respect to the 10.8cm spectrum. In the lower energy regime (<100 keV), the contents of the spectra of 16.8cm and 22.8 cm decrease with increasing sediment thickness. In the region 100-200 keV the spectra are similar to the spectrum of the 10.8 cm Zircon bed, while at energies >2MeV the spectra show a decrease with increasing sediment thickness. The precise cause of this effect is yet unknown but the energy dependence of the attenuation coefficient or effects of multiple Compton scattering could give explanations. In the experiments, the upper 10cm of the sediment consisted of a mixture of Zircon and Quartz and a thickness of pure Zircon larger than 10cm was not measured. The results in Figure 2.2 indicate that the effect of increase attenuation with increasing count rate is independent of  $\gamma$ -ray energy for a sediment thickness <10 cm. The measurements on a sediment bed >10.8 cm are excluded from further data analysis.

The results of the calibration measurements of Quartz and Zircon are plotted in Figure 2.3 to Figure 2.5. In Figure 2.3, the total count rate (where total counts represents the number of counts between 0.5-3 MeV) of Zircon for varying thickness of sediment is presented. These data show a less than linear increase of the count rate with increasing sediment thickness as a result of the interaction between the variation in count rate with changing source (increasing thickness of sediment) and self-absorption. In Figure 2.4 to Figure 2.5, the total count rate as function of sediment thickness is shown for Quartz placed on concrete (Figure 2.4) and Quartz placed on a box of Zircon (Figure 2.5). In all cases, the surrounding material (concrete and Zircon, respectively) has higher activity concentrations than the Quartz itself. This means that Quartz will mainly act as an absorber of underlying material, resulting in a negative correlation between count rate and sediment thickness. The statistical uncertainties in the total count rate are very small due to the long measuring time. However, many measurements were done on both sides of the flume. Mainly for the measurements with Zircon, the statistical uncertainties in the total count rate can not explain the spread in the data points of the duplicate measurements. It is likely that external error sources (like homogeneity of the sediment and uniformity in thickness of the sediment) are larger than the statistical uncertainties. In the procedure of changing the set-up for the duplicate measurements, part of the variables that contribute to the external error sources could have changed. The variation in these duplicate measurements is used to estimate the uncertainty due to the external error sources (resulting in uncertainties in the calibration measurements from 3-10%).

To determine the actual attenuation coefficients for Quartz and Zircon in the sediment, the calibration measurements were fitted to equation (1.11). The results of these fits are given in Table 2.2 and Figure 2.3-Figure 2.5.

Table 2.2: Results from the fit of the calibration measurements with equation (1.11)

	$L_1 \epsilon$ (counts s <sup>-1</sup> cm <sup>-1</sup> )	$\mu'_{1\rho_1}$ (cm <sup>-1</sup> )	$N_2$ (counts s <sup>-1</sup> )	$\chi^2_{red}$
Zircon	900 (100)	0.25 (0.05)	15.1 (1.4)	0.3
Quartz	0.65 (0.1)	0.125(0.015)	11.9 (0.5)	0.33
Quartz on Zircon	33 (10)	0.16 (0.01)	2490 (40)	1
Quartz on Zircon ( $L_1 \epsilon$ ) similar to quartz	0.65	0.124 (0.003)	2411 (42)	1.1

Table 2.2 shows the parameters that resulted from the fit with equation (1.10). The  $\chi^2_{\text{red}}$  values are presented as a parameter that shows the quality of the fit (see Appendix Appendix D).  $L_1\varepsilon$  is a measure of the specific activity (the activity per cm thickness) determined by the detector of the studied sediment,  $\mu'_{1\rho_1}$  is the mass attenuation coefficient times the density of the studied sediment and  $N_2$  the count rate the originates from the underlying medium (in most cases concrete, whilst in the experiment of Quartz on Zircon,  $N_2$  is the count rate coming from the Zircon).

For all measurements the  $\chi^2_{\text{red}}$  value indicates that the model describes the data well.

Table 2.2 shows that the value of the parameter  $L_1\varepsilon$  depends on the experiment. The parameter  $L_1\varepsilon$ , is correlated to the total count rate measured at an infinite thick sediment bed, or at a thickness near the “view” of the detector (see page C-5). This thickness for Quartz is estimated as 40cm. The measurements of Quartz on Zircon were only up to a maximum sediment thickness of 13 cm, much less than the maximum “view” of the detector. Therefore, the parameter  $L_1\varepsilon$  is based on extrapolation. Since the count rate ( $N_2$ ) from the underlying Zircon is very high compared to the count rate for Quartz, a small uncertainty in the extrapolation can result in a very high specific activity for Quartz. Since deviation between the specific activities of Quartz and concrete is small, it is assumed that the measurements of Quartz on concrete do give a more accurate specific activity of Quartz. This value is used for a refitting of the measurements of Quartz on Zircon. The results of this fit are also presented in Table 2.2. These results (with a  $\chi^2_{\text{red}}$  in the fit of 1.1) show that the attenuation coefficient of Quartz ( $\mu'\rho$ ) is well reproduced compared to the Quartz on concrete measurements. For further analysis the attenuation coefficient of the Quartz on concrete measurement is used.

Table 2.3: Attenuation coefficients ( $\text{cm}^2\text{g}^{-1}$ ) for Quartz and Zircon calculated from the fitted  $\mu\rho$  coefficients, the density of the sediment  $\rho_{\text{sediment}}$ , and the bulk density of the sediment ( $\rho_{\text{bulk}}$ ) assumed that the porosity of the sediment is equal to 0.36 and that the pore space is filled with water.

Sediment	$\mu'\rho$ ( $\text{cm}^{-1}$ )	$\rho_{\text{sediment}}$ ( $\text{gcm}^{-3}$ )	$\rho_{\text{bulk}}$ ( $\text{gcm}^{-3}$ )	$\mu'\rho_{\text{literature}}^{13}$ ( $\text{cm}^{-1}$ )
Quartz	0.125 (0.015)	2.4	1.9	0.10 - 0.12
Zircon	0.25 (0.05)	4.4	3.2	0.15 - 0.18

The attenuation coefficients of Quartz and Zircon are compared with values found in literature (Table 2.3, Debertin and Helmer, 1988). Since the attenuation is energy dependent, the centre of gravity of the measured energy spectra for Quartz and Zircon are calculated. The centre of gravity of the energy spectra of Quartz and Zircon are located around 1250 keV. The literature values of the mass attenuation coefficients for  $\text{SiO}_2$  ( $\rho=1.9 \text{ gcm}^{-3}$ ) are between  $0.063 \text{ cm}^2\text{g}^{-1}$  for an energy of 1 MeV and  $0.052 \text{ cm}^2\text{g}^{-1}$  for 1.5 MeV. The mass attenuation coefficient for Zircon for the given energy is deduced from the mass attenuation coefficient from Germanium, which has a similar Z as Zr. The mass attenuation coefficients for Germanium are  $0.057 \text{ gcm}^{-2}$  and  $0.046 \text{ gcm}^{-2}$  for 1 MeV and 1.5 MeV respectively. The linear attenuation coefficients ( $\mu'\rho$ ) are calculated by multiplying the literature mass attenuation coefficients ( $\mu'$ ) with the bulk density of the sediment ( $\rho$ ) see Table 2.3. This indicates that the measured attenuation coefficients of Quartz and Zircon are in the same range as the ones reported in literature.

<sup>13</sup> For energies of 1.5MeV and 1MeV, Debertin and Helmer (1989)



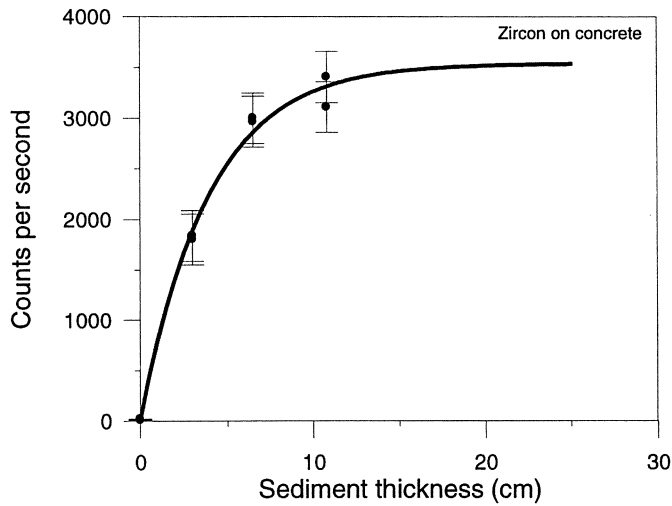


Figure 2.3: The response of total count rate (count/sec) on the thickness of the sediment bed. The uncertainties are determined from the analysis of the duplicate measurements.

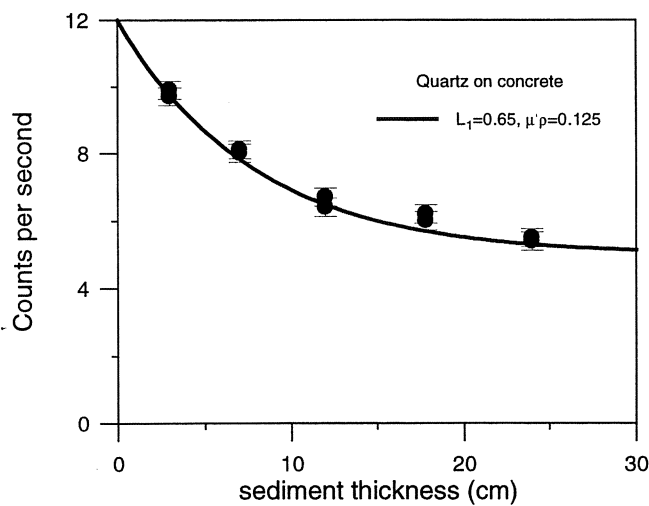


Figure 2.4: The response of total count rate (count/sec) on the thickness of the sediment bed. The uncertainties are determined from the analysis of the duplicate measurements.

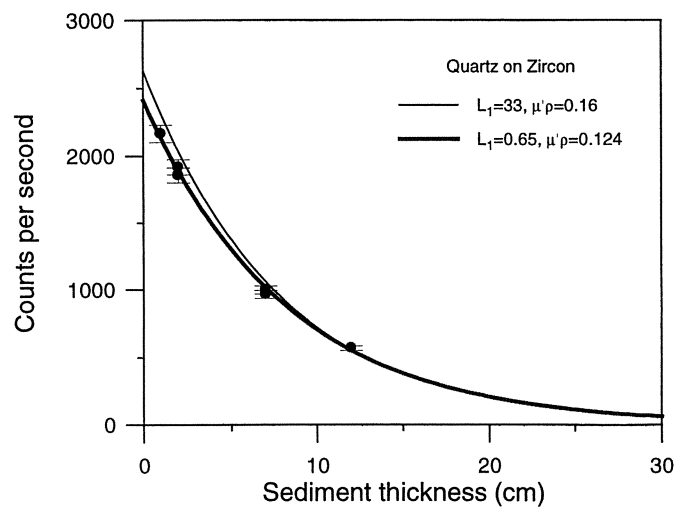


Figure 2.5: The response of total count rate (count/sec) on the thickness of the sediment bed. The error bars represent statistical uncertainties.

Since the attenuation coefficients and density of the material are known, the penetration depth (see equation (1.18)) can be calculated for pure Quartz and pure Zircon (Table 2.4). From Table 2.4 follows that the variation in maximum depth of penetration between Quartz and Zircon is a factor 2 and ranges from 24 cm for Quartz to 10 cm for Zircon, provided that a precision of 5% is needed.

Table 2.4: Maximum depth of penetration for Quartz and Zircon, for two different precisions

Sediment type	$\mu' \rho$ (cm <sup>-1</sup> )	Precision	$Z_{\infty}$ (cm)
Quartz	0.125 (0.015)	0.01	36 (4)
Zircon	0.30 (0.02)	0.01	15.3 (1.0)
Quartz	0.125 (0.015)	0.05	24 (3)
Zircon	0.30 (0.02)	0.05	10 (0.7)

### 2.1.3 Analysis of measured spectra

#### Standard spectra

The conversion from radiometry to Zircon concentrations is done by using the spectrum unfolding method as described in de Meijer et al. (1997). This spectrum unfolding calculates how often specific “standard spectra” fit in the measured spectrum. Normally, standard spectra of K, U and Th are used, but to convert the measured radiometric signal directly to zircon concentrations, standard spectra for zircon and quartz were recorded. Each standard spectrum represents an infinite bed of Zircon or Quartz and is used in the Medusa Post Analysis software (MPA) developed at KVI.

The recording of standard spectra requires that the sediment bed has an “infinite” thickness. Table 2.4 shows that for a precision of 5%, the sediment bed is infinite for Zircon at a thickness >10 ( $\pm 0.7$ ) cm and for Quartz at a thickness >24 ( $\pm 3$ ) cm. The spectrum recorded with 24 cm of Quartz and the spectrum recorded with 10.8 cm of Zircon are used as standard spectra. The calibration measurements for Zircon showed that the spectrum measured at a Zircon bed of 10.8 cm can best represent the spectrum shape of thinner Zircon beds. Therefore this spectrum is used as standard spectrum.

If, in an ideal situation, the concentration of Zircon is determined by  $\alpha \pm \delta\alpha$ , the concentration of Quartz will be determined as  $(1-\alpha) \pm \delta\alpha$ . However, since the fitting of the standard spectra is based on a  $\chi^2_{\text{red}}$  minimisation, this relation can not be added as a constraint. Absorption effects in the sediment can result in a change in shape of the spectrum compared to the shape of the summation of the standard spectra. It is possible that in this case  $\chi^2_{\text{red}}$  is minimised by summing concentrations of Quartz and Zircon that do not satisfy above described relation. Since the activity concentrations of Quartz and Zircon vary by a factor 100, changing the concentration of Quartz will effect the calculated spectrum and  $\chi^2_{\text{red}}$  less than a change in the Zircon concentration. This effect can lead to physically incorrect concentrations of Quartz. Therefore, only Zircon concentrations will be determined by the spectrum deconvolution and quartz is gained by calculating  $(1-m_{\text{zirc}})$ .

## Variation of background

The radiometric measurements of the experiments with pure Quartz are used to deduce variations in background radiation as a function of x-position in the flume. Figure 2.6 shows the total count rate measured on the d-side of profile A901 (the profile recorded after experiment A901). In the part of the flume between  $x=10\text{m}$  and  $x=20\text{m}$ , the sediment thickness increases from 0.5 mm to 30 cm. Since the activity concentration of Quartz is lower than the activity concentration of the surrounding concrete, the decreasing trend of count rate from  $x=10\text{m}$  to  $x=20\text{m}$  is the result of increasing absorption from the background radiation. The increased radiation level around  $x=30\text{m}$  is caused by the concrete measuring cabin which is placed over the flume.

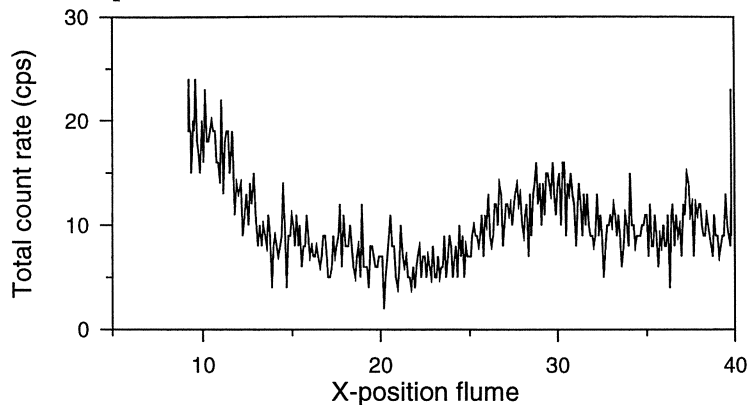


Figure 2.6: Variation in total count rate due to changes in background as a function of position in the flume. The measurements were conducted on profile A901

The background radiation along the flume is not constant. For the variations caused by the absorption with increasing sediment thickness, corrections are made in the analysis procedure, but variations of 10 cps occur due to the concrete cabin. However, since the activity concentrations of the bed with Zircon are high ( $\sim 3000\text{ cps}$ ) these small changes in background radiation ( $<0.5\%$ ) fall within the statistical uncertainties and are ignored.

## 3 Validation & calibration of the model

In chapter 1.3, assumptions are made for the parameterisation of the relation between the measured count rate on top of the bed and the concentration of Zircons that are present in the sediment. Chapter 2.1.2 shows that a 1D model can describe the effect of sediment thickness on the measured count rate only to a maximum sediment thickness. Next paragraph focuses on the validation of the other assumptions that were made.

### Energy dependence of the mass attenuation coefficient and build-up

Two of the assumptions that were made in chapter 1.3, comprised effects of build-up and the energy dependence of the attenuation coefficients. Chapter 1.3 stated that build-up and the energy dependence of the attenuation coefficients can be parameterised in effective coefficients.

The results of chapter 2.1.2, indicate that for Zircon sediment with a thickness larger than 12 cm, the attenuation coefficient is dependent of energy. In the experiments, the sediment will be mixed and most of the sediment is composed of Quartz with a maximum thickness of 10 cm. Measurements are done to test these effects in case the sediment is composed of pure Quartz. Therefore, layers of Quartz with varying thickness were placed on a box of Zircon and the  $E_\gamma$ -spectra were recorded. Figure 3.1 shows the  $E_\gamma$ -spectra of the varying Quartz layers divided by a pure Zircon spectrum. In a situation where effects of build-up and the energy-dependence of the attenuation coefficient are negligible, the spectra will have a shape similar to the pure Zircon spectrum and the spectra divided by the spectrum of Zircon will be a horizontal line. The results in Figure 3.1 show that in the energy range between 0 and 0.5 MeV, large effects occur but in the range of 0.5 and 3 MeV, spectra are almost horizontal with only small variations. Although the spectra are almost horizontal, the general trend of the spectra shows a slight slope that decreases with increasing thickness of Quartz. For an elaborate discussion on these slight changes in shape with varying thickness of Quartz, present knowledge is not sufficient and Monte Carlo simulations are needed. This discussion and simulations fall beyond the scope of this report, but the results show that the effects of build-up and energy dependence of the attenuation coefficient in a Quartz covering are small in the range and can be neglected in the parameterisation of these experiments.

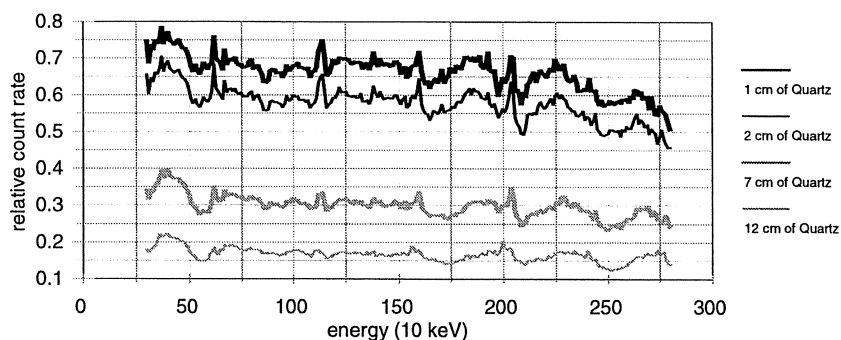


Figure 3.1:  $E_\gamma$ -spectra divided by a spectrum of pure Zircon, for the measurements with varying thickness of Quartz on 12 cm of Zircon.

### Build-up from water

The detector is towed from the dry part of the beach towards a water depth of 70 cm. When the detector is above the waterline, the solid angle (the surface of sediment that can be detected by the system) will be larger than when the system is fully surrounded by water. Moreover, the water mass will cause scattering of photons. These effects will mainly result in an increase of the Compton part of the spectrum. Figure 3.2 shows the lower part of the spectrum (0-1.5 MeV) for measurements at a water depth 0-0.1 m and measurements at water depth 20-30 cm. It is clear that effects on the Compton edge due to the changing water depth occur, but only in the channels 0-30 (energy range 0-0.3 MeV). It is remarkable that for the measurements of Quartz on Zircon the effects on the Compton continuum occur in almost a similar region. Therefore, these channels are omitted from the data analysis and the spectra are unfolded in the range of channels 50-250 (energy range 0.5-2.5 MeV).

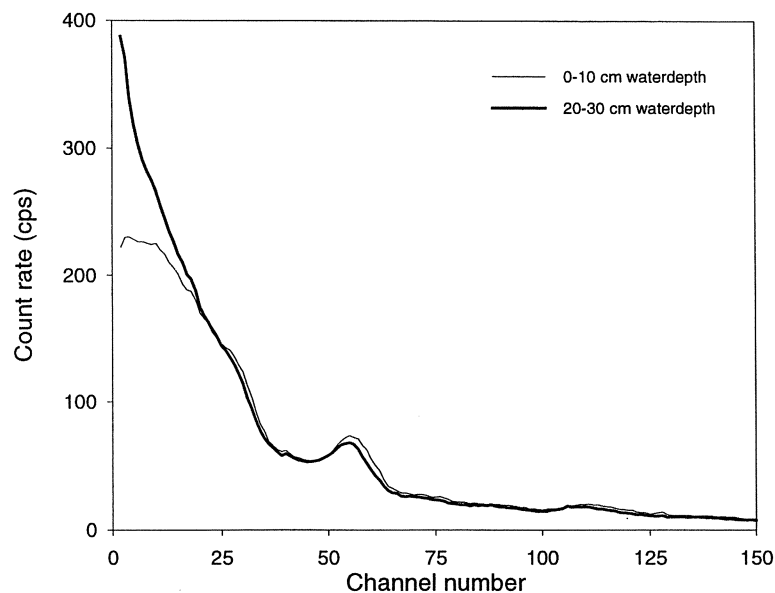


Figure 3.2: Differences in count rate at different water depths. The signal at from 20-30 cm water depth shows an increased count rate at lower channel numbers due to scattering of  $\gamma$ -rays in the water

## 4 Validation of the calibration

The description of the model and the calibration measurements showed that the processes that are involved in *in situ*  $\gamma$ -ray measurements are complex and only partly understood. The model description aims at a very accurate depth-dependent description of the sediment composition in the upper layer. Although the calibration measurements were done as accurate as possible, the processes involved are so complex and the measurements difficult (e.g. under water, sediment dispersion, porosity changes) that a validation of these parameters is necessary. However, these calibration measurements do give insight in the range of the parameter values. To get a better grip on effects of possible uncertainties in the mass attenuation coefficients for Quartz and Zircon and the thickness of layer  $L_2$  (see Figure 1.7), a sensitivity analysis is conducted with the model. Moreover, sediment samples that were derived from the final profile of the C-experiments are used to “tune” the model, such that the Zircon distribution measured with the sediment samples is determined well. The sediment samples were taken from profile C404 and were derived from varying depths in the sediment.

### Sensitivity analysis of the radiometric data-analysis

To determine the effect of variations in the coefficients that are used in the model, the radiometric signal is analysed with variations in  $\mu'\rho_{\text{quartz}}$ ,  $\mu'\rho_{\text{zircon}}$  and  $L_2$ , with an upper layer thickness of 5cm. The upper layer thickness of 5cm is the maximum sediment accumulation +1cm. The results of these analyses and the Zircon concentrations that are estimated from sediment samples are presented in Figure 4.1 to Figure 4.3.

Figure 4.1 shows the calculated Zircon concentrations as function of distance over the profile. The influence of variations in the attenuation of Zircon is of course largest for those regions with high Zircon content. Compared to the Zircon concentrations of the sediment samples, the

Zircon concentrations are underestimated in the region between  $x=10-24\text{m}$  for the linear attenuation coefficients  $>0.154\text{ cm}^{-1}$ . In the region between  $x=24-40\text{m}$ , the results with the attenuation coefficient measured in the calibration procedure fit well to the Zircon concentrations of the samples. A smaller attenuation coefficient results in the region  $x=24-40\text{m}$  in an overestimation of the Zircon concentration. A larger attenuation coefficient of Zircon results in an underestimation of the Zircon content. All curves underestimate the Zircon concentration between 20 and 25 meter.

The effects of variations in the attenuation coefficient of Quartz are shown in Figure 4.2. Decreasing the mass attenuation coefficient by  $0.05\text{ cm}^{-1}$  has a dramatic effect and results in an underestimation in the Zircon concentrations along the entire profile. Increasing the attenuation coefficient by  $0.05\text{cm}^{-1}$  results in an increase in the calculated Zircon content. This increase is larger for lower Zircon concentrations. In general, increasing the linear attenuation coefficient of Quartz by  $0.05\text{cm}^{-1}$ , gives a better fit to the results of the sediment samples.

Before the sediment mixture was brought into the flume, the upper 10cm of the pure Quartz bed were removed and replaced with the sediment mixture. This procedure was done by hand and it is almost impossible to have a constant thickness of the sediment mixture ( $L_2$ ) of 10cm. Observations showed that the total thickness of the sediment mixture can vary  $\sim 2\text{cm}$ , resulting mainly a smaller sediment thickness than 10cm. The effect of these variations of the thickness of  $L_2$  on the calculated Zircon concentration is shown in Figure 4.3. These analyses show that the effect is more pronounced in the region with higher Zircon concentrations, but at the locations where the Zircon concentration is small ( $<10\%$ ) the variation of layer  $L_2$  has not effect. An increase in the thickness  $L_2$  results in a lower calculated Zircon concentration, decreasing  $L_2$  results in higher Zircon concentrations. Variations in  $L_2$  do not seem to improve the fit to the Zircon concentrations from the sediment samples. An overestimation of the thickness of the active layer will result in an underestimation of the Zircon concentration of maximum 10% (absolute), but these effects are largest in the region with high Zircon concentrations. However, the sensitivity analysis shows that the model is more sensitive to uncertainties in the attenuation coefficients than to an inaccurate estimation of the thickness of layer  $L_2$ .

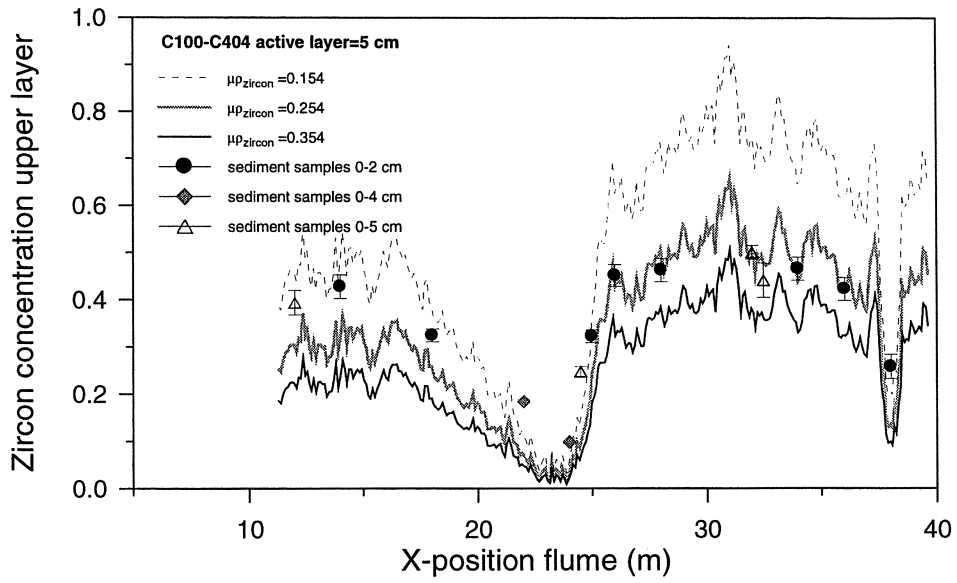


Figure 4.1: The effect of varying attenuation coefficients  $\mu_{\text{zircon}}$  ( $\text{gcm}^{-2}$ ) of Zircon on the Zircon concentration in the upper layer of profile C404.

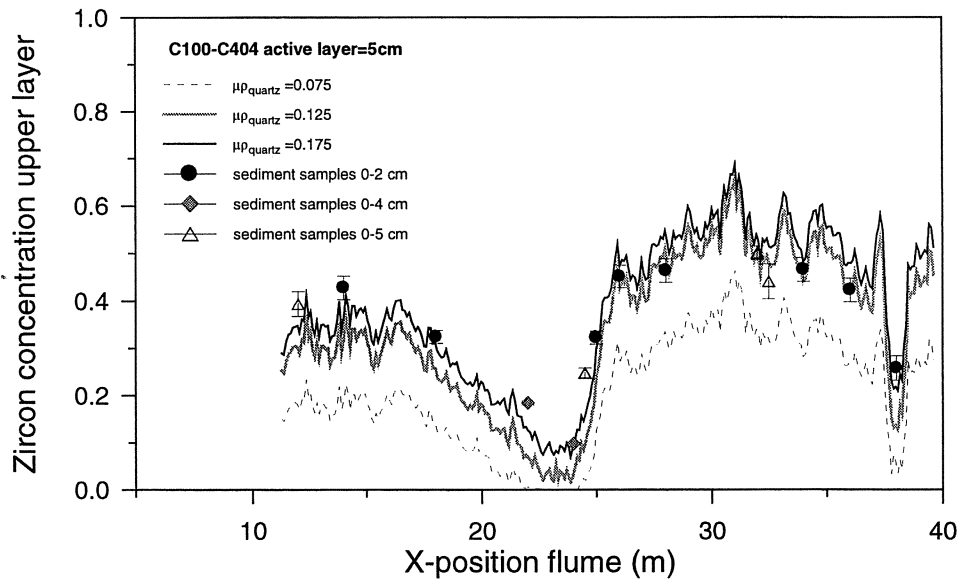


Figure 4.2: The effect of varying attenuation coefficients  $\mu_{\text{quartz}}$  ( $\text{gcm}^{-2}$ ) of Quartz on the Zircon concentration in the upper layer of profile C404.

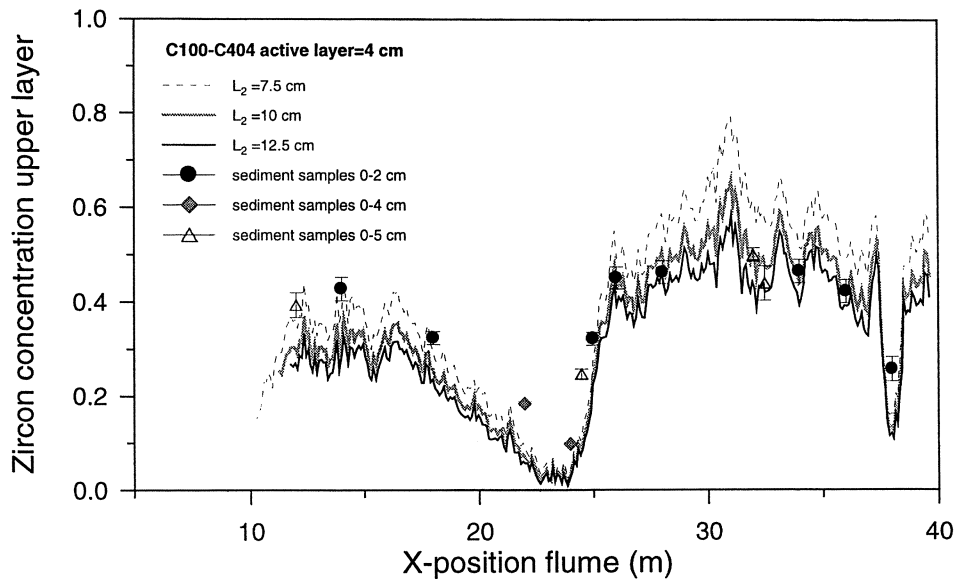


Figure 4.3: The effect of varying thickness of layer  $z_2$  on the Zircon concentration in the upper layer of profile C404.

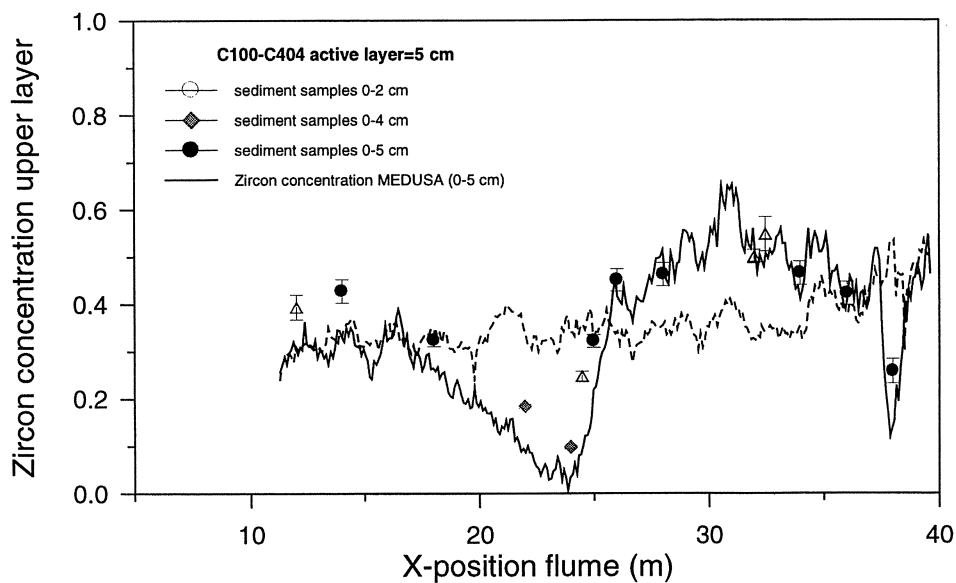


Figure 4.4: Zircon concentration in the upper 5 cm of the sediment measured with the MEDUSA system at the beginning of series C (dashed line) and on profile C404 (solid line) and Zircon concentrations of sediment samples from varying depth. The attenuation coefficients are according to Table 2.3,  $L_2=10$  cm.

### Comparison with sediment samples

A comparison between the calculated Zircon concentrations from the MEDUSA signal and the measured Zircon concentrations in the sediment samples (Figure 4.4) shows that between  $x=25$  and  $x=40$  m, the samples are well described by the MEDUSA measurements. However, in the range between  $x=10$  and  $x=25$  m, the Zircon concentrations of the final profile are



underestimated. Moreover, according to the MEDUSA measurements the mean Zircon concentration (by weight) of the initial profile is 36%, while the sediment mixture was composed of 44% of Zircon. This indicates that the calibrated parameters are probably not correct. Figure 4.4 shows that the underestimation of the Zircon concentrations occurs in the region with small Zircon content. The sensitivity analysis learned that increasing attenuation coefficient of Quartz increases the Zircon concentration in the region with a low Zircon content, but hardly influences the Zircon concentration in the region of 50% of Zircon. Therefore, the fit is optimised by changing  $\mu' \rho_{\text{quartz}}$ . This resulted in an attenuation coefficient of Quartz of  $0.18 \text{ cm}^{-1}$  (Figure 4.5).

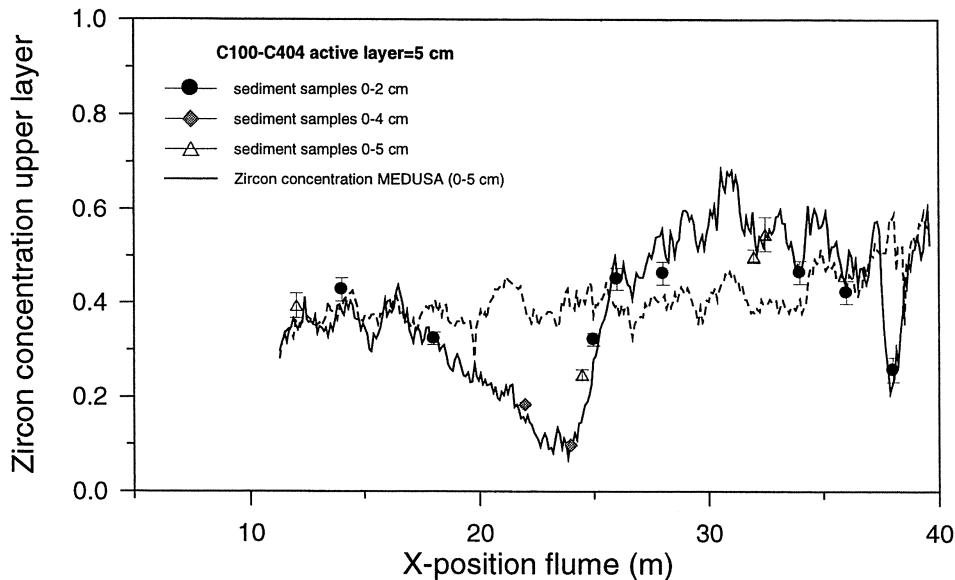


Figure 4.5 Zircon concentration in the upper 5cm of the sediment measured with the MEDUSA system at the beginning of series C (dashed line) and on profile C404 (solid line) and Zircon concentrations of sediment samples from varying depth. The fit is optimised by changing  $\mu' \rho_{\text{quartz}}$  to  $0.18 \text{ cm}^{-1}$ ,  $\mu' \rho_{\text{zircon}}=0.25 \text{ cm}^{-1}$  and  $L_2=10 \text{ cm}$ .

The results in Figure 4.5 show that the calculated Zircon concentrations can well describe the measurements. Also the average Zircon concentration in the upper layer of the initial sediment bed (41% by weight) correspond rather well to the Zircon concentration of the initial sediment mixture. The coefficient  $\mu' \rho_{\text{quartz}}$  is 50% larger than the reported values from literature (Table 2.3). This deviation corroborates the measurements of  $\mu' \rho_{\text{zircon}}$ , that were 40% larger than the literature values. The larger attenuation coefficients compared to the literature ones are the result of 3D effects.

## 5 Conclusions

Detailed investigations on calibration measurements indicated that the relation between the measured radiometry on top of the sediment bed and the Zircon concentration of a layer with known thickness can be described by a 1D model. To determine the inaccuracy of the model coefficients from the calibration measurements, the resulting Zircon concentrations from the model are compared with results from sediment sampling. This comparison indicated that by adjusting one of the model coefficients, the deviation between Zircon concentration from the samples and Zircon concentrations from radiometry can be decreased to <5%.

## 6 References

de Meijer, R. J., Stapel, C., Jones, D. G., Roberts, P. D., Rozendaal, A. & Macdonald, W. G. (1997) *Improved and New Uses of Natural Radioactivity in Mineral Exploration and Processing*. *Exploration Mining Geology*, 6(No.1), pp. 105-117

Debertin, K. & Helmer, R. G. (1988) *Gamma and x-ray Spectrometry with semiconductor detectors*.

# Appendix D .

## I The meaning of uncertainties and $\chi^2_{\text{red}}$

In the report, the  $\chi^2_{\text{red}}$ -value is used to estimate the quality of models that are used to describe the data. This section discusses some informative background considering uncertainties and the  $\chi^2_{\text{red}}$ -value connected to weighted means calculations or weighted fitting procedures.

Performing repeated measurements of an observable never results in exactly identical values, but the measurement results will scatter according to a certain distribution. The centre of this distribution is generally taken as the estimate of the ‘true’-value. The width of the distribution is a measure for the uncertainty that can be assigned to each measurement. For many situations, the only way to obtain insight in the uncertainty is by measuring repeatedly to obtain information of the spread and calculate the standard deviation of the measurements.

For many physical-measuring devices, these uncertainties are known a priori, because of the ‘expert’ knowledge of the device. In these cases, a measurement does have to be repeated, as the uncertainty is already known. Mathematical methods can be used to ‘propagate’ these errors for parameters that are not directly measured, but result from mathematical calculations. This procedure also includes the merging of uncertainties from different measuring devices.

Further data analysis can be based on the knowledge of these uncertainties. Values with large uncertainties have little weight in model calibrations, fits or averages, values with small uncertainties much more. The validity of these procedures or assumptions can be checked by the  $\chi^2$ -test. This test estimates the probability of an observed deviation between the data set and the model (like a weighted average or a regression line) based on the uncertainties in the data set, the number of independent observations and the degrees of freedom in the model. The test can be used to reject a model, when the scattering of the data is too large compared to the specified uncertainty. Vice versa, the test can indicate that the uncertainty specified is too small compared to the variations in the measurements. The  $\chi^2$  test can only be used when the uncertainties are Gaussian or Poisson distributed.

The  $\chi^2$  statistic of a data-set of measurements with size  $n$ , can be described by:

$$\chi^2 = \sum_{i=1}^n \left( \frac{y_i - f(x_i)}{\sigma(y_i)} \right)^2,$$

where  $\sigma(y_i)$  is the uncertainty in the measured parameter.. The optimal value of  $\chi^2$  depends on the number of degrees of freedom of the problem. The reduced  $\chi^2$ -value, ( $\chi^2_{\text{red}}$ ) is used as a shortcut for the full  $\chi^2$ -test, and is defined as  $\chi^2$  divided by the number of degrees of freedom (F):

$$\chi^2_{\text{red}} = \frac{\chi^2}{F}.$$

In this approach,  $\chi^2_{\text{red}}$  should be close to unity when the variability is properly expressed by the specified uncertainty. When the  $\chi^2_{\text{red}}$ -value is not equal to unity and when it is suspected that the uncertainty is underestimated and the use of a model to describe the data is justified, the uncertainty of the final result can be multiplied by the square root of the  $\chi^2_{\text{red}}$ -value. With this method a reasonable estimate for the uncertainty in the final result is obtained. The uncertainty calculated from the measurement errors with the model prescription is called the internal uncertainty, whereas the uncertainty incorporating the quality of the model fit, after multiplication with the square root of the  $\chi^2_{\text{red}}$ -value is called the *external* uncertainty.